Aluminium-Palladium Transition Edge Sensors

by

Lauren Margaret Persaud

A thesis
presented to the University of Waterloo
in fulfillment of the
thesis requirement for the degree of
Master of Science
in
Physics

Waterloo, Ontario, Canada, 2008

I hereby declare that I am the sole author of this thesis. This is a true copy of the thesis, including any required final revisions, as accepted by my examiners.

I understand that my thesis may be made electronically available to the public.

Lauren Persaud

Abstract

A superconducting Transition Edge Sensor (TES) can be used to make the most sensitive thermometer which operates in a very narrow temperature range. The thin film bi-layer fabrication details are discussed as well as application in condensed matter physics. These include: measurement of quasi-adiabatic latent heat of superconducting transition, cobalt thermometry and photon detection.

Acknowledgements

Thanks to my advisor Professor Jan Kycia and the Low Temperature Lab Group: Chas Mugford, Jeffrey Quilliam, Nat Persaud, Shuchao Meng, Jeff Hill, Tatjana Hahlen, Patrick de Perio, Tegan Wiebe and Borko Djurkovic. Thanks to JQ for all his work setting up the ^{3}He fridge. Thanks to Chas for all his insight, knowledge and help with the latent heat setup and measurements. Thanks to Jan Kycia, Rob Hill, Gunter Scholz and David Hawthorn for being part of my committee.

To Mom, Dad, Carrie, Dave, Leah, Drew, Steve, Kristal, Grace, Eva and Beth: thanks so much for always being there and your support always.

Nat for all your encouragement, love and patience.

Contents

List of Tables

List of Figures

Chapter 1

Introduction to Transition Edge Sensors (TES)

1.1 Transition Edge Sensors

A superconducting transition edge sensor (TES) can be used to make an extremely sensitive thermometer which operates in a very narrow temperature range ($< 5\ mK$). A TES takes advantage of the sharp transition from normal state resistance (R_N) to the superconducting state. The general characteristics of the TES transition curve can be seen in Figures 1.1 and 1.2. Within this transition a very small variation in temperature corresponds to a large change in resistance. When the sensor is thermally balanced at the transition temperature, it can be used to detect very small heat or energy fluctuations. In order to select an operating temperature, a TES is fabricated as a thin film of normal metal over a thin film of superconducting metal. Due to the proximity effect [4], the relative thickness of each metal determines the critical temperature of the bi-metal.

1.2 Motivations for using a TES

A TES has many advantages over classic thermometers. The small size of a TES is useful when working in low temperature physics research where space is limited, such as in dilution refrigerators and other cryogenic apparatus. A TES is highly sensitive to variations in temperature. The devices fabricated in our lab are able to measure a change in energy on the order of 10^{-19}J, which is many orders of magnitude better than conventional techniques, such as doped germanium resistors [5]. High accuracy is necessary for sensitive measurements, as well as low noise. The devices made in our group, as part of this thesis, have a noise sensitivity of of less than $\frac{1nK}{\sqrt{Hz}}$. A TES can be used anywhere that high energy sensitivity is required. It can be used as a calorimeter to measure a heat change or as a bolometer to detect power absorption. Applications that already make use of a TES include high resolution x-ray spectroscopy [6] [7] [8], an x-ray micro-calorimeter for x-ray astronomy and material analysis [9] dark matter searches [6], and neutrino, photon and particle detectors [6] [10] [11]. Details of some of these applications will be discussed in Chapter 3.

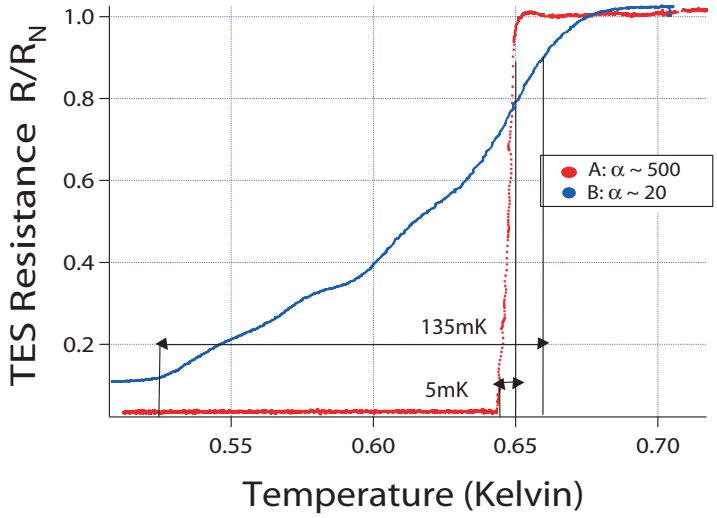

Figure 1.1: Sensitivity and transition width comparison of two TES's.

1.3 Characteristic Parameters

A TES can be described by four characteristics: the critical temperature (T_C), the normal state resistance (R_N), the transition width and the alpha parameter (α).

The T_C is defined as the temperature at the midpoint of the transition. This is used to determine if the TES is suitable for a specific application, as it can only operate in a limited temperature region near T_C.

The R_N is defined as the resistance of the device in the normal state. This is also used to determine the suitability for a specific application, as different applications may require small or large resistances for impedance matching.

The transition width is defined as the temperature range in which the sample resistance varies from $0.1\ R_N - 0.9\ R_N$. The transition width can be as low as a few mK. Depending on the application in which a TES will be used, a larger or smaller transition width may be desirable. A larger transition width may be desirable for working over a temperature range larger than a few mK. Figure 1.1 compares two TES devices with different characteristics, a drastic difference in transition width and slope is observed. The TES with the steeper slope (which corresponds to a higher alpha value) is more sensitive. Theoretical minimum transition widths are calculated using the normal state resistance and critical temperature: $\Delta T \approx T_C * 0.17 * R_N/R_C$ where R_C is the characteristic resistance [12], for $R_N = 1\ \ \Omega$, $T_C = 100$ mK and $R_C = \hbar/e^2$, the calculated transition width is 4 μK , rather than the 1 mK typically observed. The higher observed transition width is likely due to material characteristics. This work partly focuses on the fabrication details to create high α.

α is a dimensionless coefficient which defines the sharpness and sensitivity of the superconducting-to-normal transition. This dimensionless temperature coefficient is a function of bias current, applied magnetic field, and temperature (bias point) within the phase transition. Practical values found in today's literature, are in the range of 40-500 [13] [14] and have been found to be as high as 2500 [15]. The higher the value of α, the more potentially sensitive the device. This will be discussed further in Section 1.6.

1.4 Tuning T_c using the Proximity Effect

The term proximity effect is used to describe a phenomenon that occurs when a superconductor (S) is placed in contact with a 'normal' (N) non-superconductor. Typically this suppresses the T_C of the superconductor and signs of weak superconductivity appear in the normal material. This effect is caused by diffusion of Cooper pairs into the normal material, reducing the pair density in the superconductor and lowering the transition temperature [4] [11].

It is important that the electrical contact between N and S be very good. If a thin insulating layer of impurities exists at the interface, the bi-metal will not show any signs of suppressed T_C [4]. Proximity effects are much larger for normal metals which are magnetic [4], and are weakened if either S or N are 'dirty' materials. Dirty materials shorten the mean free path of the material which makes the bi-metal less prone to diffusion [4].

The proximity effect was used to set the T_C of each TES that was fabricated. A TES consists of two thin films fabricated on top of one another on a silicon wafer (see Section 3.1 for full fabrication procedure). The design was lithographically patterned in photo resist spun on the wafer, which was then RF sputtered with a thin aluminium film and an even thinner film of palladium. These two metals were sputtered without exposure to oxygen to prevent an oxide barrier from forming on the aluminium.

The T_C of aluminium is 1.2 $Kelvin$. Bulk aluminium will superconduct at the same T_C. For thin films of aluminium which have a thickness less than the coherence length (aluminium coherence length: $\xi_0 = 1600\ nm$ [16]), any additional thickness made up of normal metal will lower the transition temperature. The total thickness of the bi-metal must be less than the coherence length of the superconducting element [12] in order for the normal metal to suppress the T_C. As the ratio of normal metal to superconducting metal is increased, the T_C will continue to decrease. The theoretical T_C can be determined from Usadel theory and is discusses in Martinis's work [17]. This theory is a guide for fabrication, the real measured T_C and transition width are highly sensitive to fabrication parameters such as rate of deposition, temperature of substrate and target and the pressure

of gas in the sputtering system. For this thesis, these parameters were either varied or held constant to determine sensitivities.

1.5 Readout Techniques

The most effective readout technique for TES sensors is negative electro-thermal feedback (ETF) [6]. To implement ETF, the TES is thermally connected to a reservoir at a temperature lower than T_C. The TES is voltage biased to a position on the transition curve, causing Joule heating ($Power = \frac{V^2}{R}$) such that the temperature of the TES equals the set point of the feedback. When a rise in resistance occurs in the TES, joule heating power is inversely proportionately with the resistance change, thereby stabilizing the temperature of the TES and returning to the set point. The measurement signal is then the change in current through the TES.

Positive ETF occurs when the sensor is current biased, ie. a constant current is applied. The joule heating is calculated by: $Power = I^2R$. When a rise in resistance occurs in the TES, a proportionally larger joule heating occurs. This results in an additional rise in resistance which creates a run away effect. For this reason, the dynamic range is much smaller than the negative ETF method.

Negative ETF with a SQUID readout was first used by Irwin in 1995 [6]. The change in Joule power provided feedback that held the film at a constant temperature. The energy detected by the TES was measured by a reduction in the feedback Joule heating. Using a SQUID with ETF improved the resolution, linearity and dynamic range of the TES.

Positive ETF (current biasing) method was used by Lee *et.al.* in 1993 [18]. They correlated the voltage increase due to phonon absorption to the area of the sensor which was driven normal and the energy depth deposited in the substrate. Their TES consisted of 400 parallel lines. By knowing the amount or area of the TES which went normal they were able to determine the type of phonon activity.

Detailed descriptions of many readout options will be discussed in Chapter 4 including current biased, voltage biased, use of SQUID and Low Temperature Transformer (LTT).

1.6 Sensitivity

For a negative ETF setup one would assume that the ideal operating point of a TES is the mid point of the transition, where the slope of the transition is the highest. In fact the alpha parameter is not constant across the $N-S$ transition, but there is a maximum found in the lower half of the transition illustrated in Figure 1.2. TES's are typically operated at $25\%R_N$ where α is near its maximum. Alpha is the fractional change in resistance over the fractional change in temperature. It is a very effective parameter for comparing different sensors and is defined by Equation 6.1.

$$\alpha \equiv \frac{dR}{R} \Big/ \frac{dT}{T} = \frac{dlogR}{dlogT} \tag{1.1}$$

Where R is the resistance and T is the temperature [12],[13].

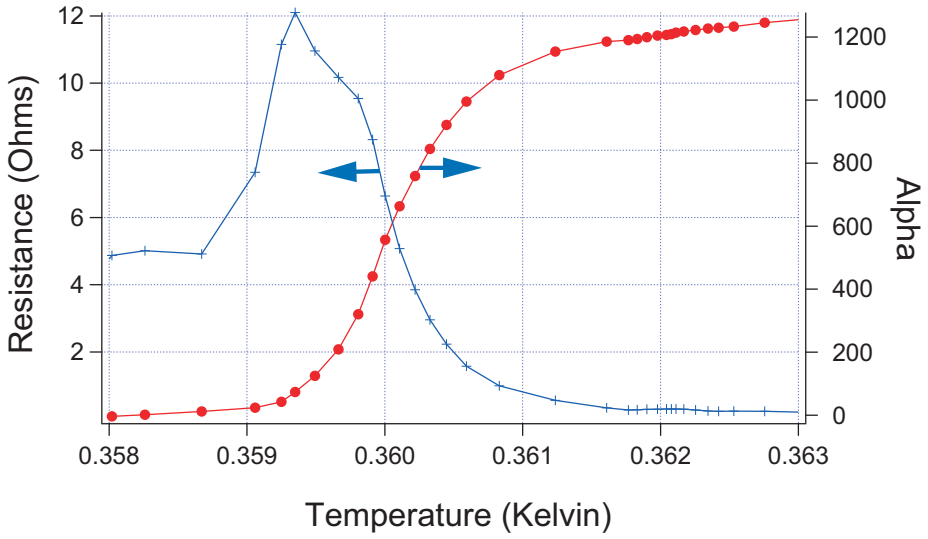

Figure 1.2: Alpha (blue) and resistance (red) as a function of temperature for a TES.

It can be seen that alpha effects positive and negative ETF differently. For positive ETF (constant current biased), the power is I^2R and the power scales with resistance. For any α, the ideal bias point is around the half way point, at $50\%R_N$, Since saturation is a a potential draw back, there is a smaller fractional change of power as a heat pulse is detected. For example, using the data from Figure 1.2, if initially biased at the 1 Ω point, the heating due to the excitation current to run the TES is that which results in a 100 mK temperature difference between the stage and the TES. For a detected heat pulse of 0.5 mK, the TES resistance increases to approximately 5 Ω, and the power increases five times. This results in a temperature difference between the stage and the TES five times larger than the initial 100 mK and saturated far into the normal region. Now if biased at the half way point, initially biased at 5 Ω, a 0.5 mK heat pulse would bring the TES resistance to 9 Ω. This is a 9/5 times power increase resulting in a temperature difference of only 180 mK. Now although in both these cases the TES would have resulted in saturation, if one was anticipating much smaller heat pulses, it is clear that there is less possibility of saturation for $50\%R_N$ than at $25\%R_N$ even though there is not as large an alpha. Alternatively, for negative ETF (constant voltage biased), the bigger the alpha the better since a small percentage change in heat results in a small percentage change in temperature. Since the power is $\frac{V^2}{R}$ this converts to a larger percentage change in heat produced by the excitation (due to lower heating, making the TES stable). It is obvious that the ideal operating point is lower than $50\%R_N$ since R is in the denominator for the power calculations, only a minor resistance change is necessary for large readout.

From Fraser's work, the largest alpha parameter possible for a given sensor is dependent on the sensor's room temperature resistance value and the two dimensional characteristic resistance, as shown in Equation 1.2 [12].

$$\alpha_M = \frac{23.5 R_C}{R_N} \tag{1.2}$$

A maximum sensitivity for a given TES with $R_N = 1\Omega$ would provide an upper limit for α of 10^5. Figure 1.1 shows the temperature-resistance curves for two sample TES's and it is noted that the steeper transition corresponds to a higher alpha value. In order to easily compare the sensitivity of a TES to other common thermometers, many types of thermometers are plotted in Figure 1.3.

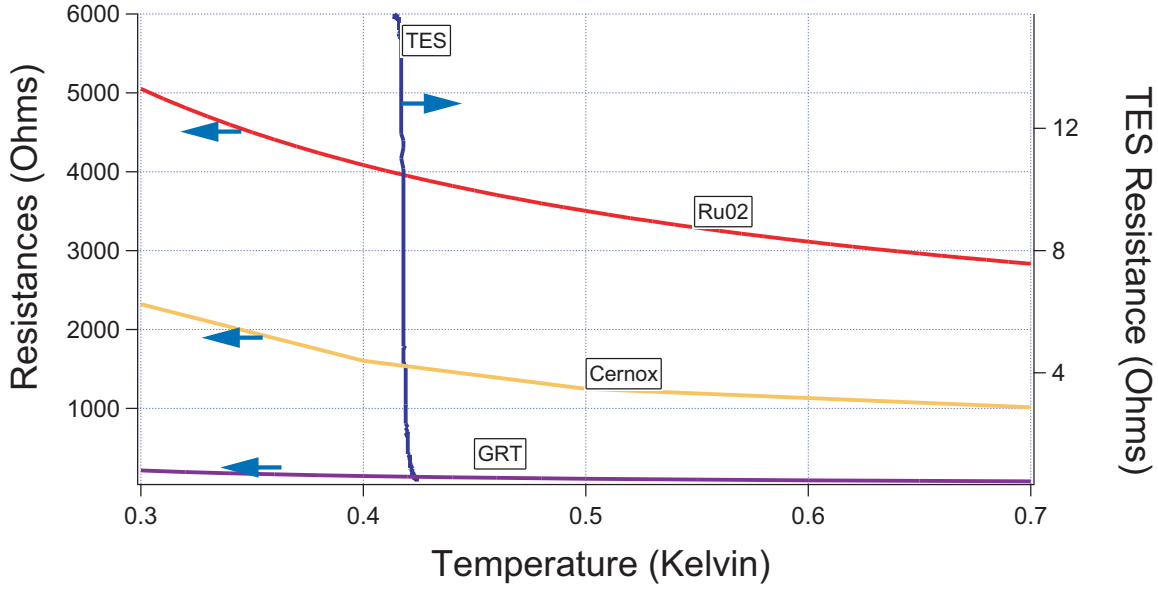

Figure 1.3: Comparing the sensitivity of a TES with Germanium resistor, Cernox and Ruthenium Oxide thermometers.

1.7 Background Work

TES's are made by many groups and with many different materials. The materials and some characteristics of TES's from some other groups, as well as Waterloo, are presented in Table 1.1. It is interesting to note that the coherence length for all superconducting materials is quite large. This is important since the total thickness of the bi-layer must be less than the coherence length. Niobium was briefly considered when making sensors at the University of Waterloo. The likely reason why niobium was never used here or elsewhere to make TES's is its coherence length is 38 nm. It would be very difficult to create accurate thin films at such a low total thickness. We chose to work with Al-Pd for several reasons. Firstly, these two metals have already been loaded in our sputtering system to fabricate SQUIDs. Aluminium and palladium are used in SQUID fabrication for their characteristics to form high quality films (grain structure and uniformity). The T_C of aluminium is relatively low, requiring little proximity coupling effect for reducing the T_C. The coherence length is long, allowing for deposition of relatively thick films. The binary phase diagram for Al-Pd shows that they do not easily form a compound at room temperature which is shown in Figure 1.4 [1]. Investigating the binary phase diagram of metals would be a good method to determine appropriate material combinations as it is important to know at what temperatures different compounds may form and change the bi-layer structure. NIST found that molybdenum-copper TES's had good long term stability to inter-diffusion and corrosion and that the long electron mean free path in copper provides fast diffusion of heat. Aluminium-silver TES's were found to degrade over time [9].

Table 1.1: Material comparison.

Elements	T_{C-S} K	T_{C-TES} K	α_{TES}	ΔT_{TES} mK	Coherence length nm	Location Location
Al - Pd	1.2	0.295-1.466	2-7200	1-575	1600	Waterloo
Ir - Au	0.112	0.0395	0.3	5	4400	Max Planck Institute [11]
Mo - Co	0.92	0.093				NIST [9]
Al - Ag	1.2				1600	NIST [9]
Ti	0.39				800	Stanford [18]
W	0.015				300	NIST [6]

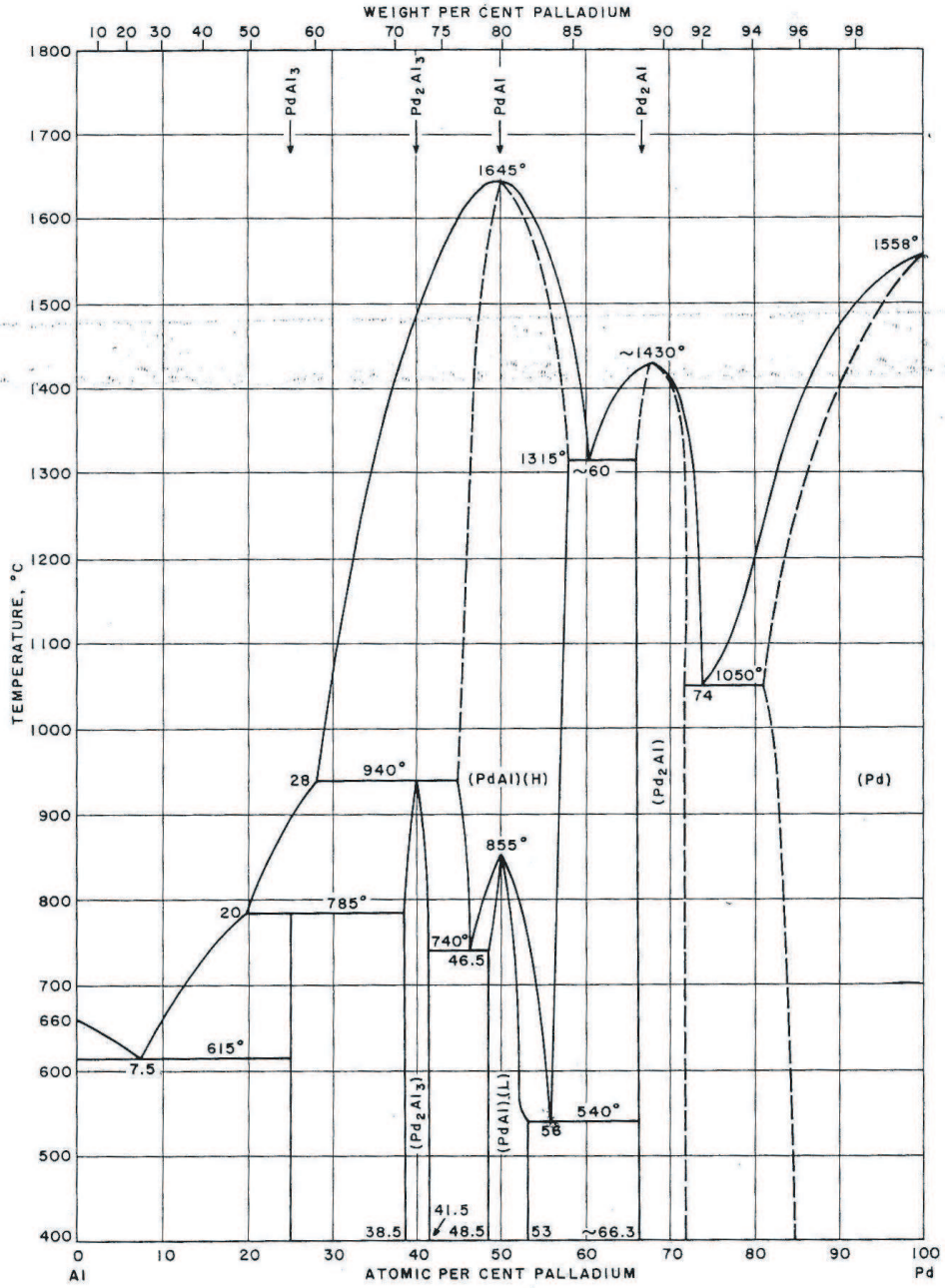

Figure 1.4: Aluminium-Palladium binary phase diagram [1].

1.7.1 Historical overview of TES sensors

One of the first ever TES applications was a thermal detector used as an x-ray spectrometer by Moseley *et.al.* in 1984 [7]. The experimental setup consisted of an energy absorber, semiconductor thermometer and support structure making up the bolometer components. Using the TES in a voltage biased setup, small variations in voltage were measured. This work models the detector as an absorber with an attached temperature sensor (TES). All characteristics have been calculated and discussed in their paper. Their TES had an alpha value of 4 and operated at a temperature of $100mK$. This thermal detector was a breakthrough in detectors as it was able to offer the high efficiency of solid state detectors and the resolution found in a dispersive spectrometer.

An example that highlights how TES's have improved for bolometer applications is the SCUBA-2 (Submillimetre Common-User Bolometer Array) Project. SCUBA had two of the most versatile and powerful submillimetre cameras of its time in 1987 [5]. This detector used neutron transmutation doped germanium as the thermometer component of the bolometer, and a feedhorn to enhance efficiencies. This is a mechanical system where each pixel was constructed individually with the option to later replace single pixels throughout lifetime of the detector. One camera worked at $850\mu m$ with 37 pixels and the other worked at $450\mu m$ with 91 pixels. Each pixel was composed of a single bolometer. The total sensitivity was $10^{-15}W/\sqrt{Hz}$. The second generation camera, SCUBA-2, is an improvement of 11872 additional pixels and operates up to 1000 times faster than SCUBA [19]. The major difference between these two detectors is the move from doped germanium thermometers to TES's with SQUID readouts. The fabrication differences can be seen in Figure 1.5 [2]. The use of TES/SQUID results in high sensitivity and excellent feedback modes and can operate faster than conventional bolometers of the same thermal properties. Also, much less insensitive area exists due to the required dimensions of thin film fabrication technology versus mechanical feedhorn technology on SCUBA. It was necessary, for practical wiring issues, that the large number of pixels in SCUBA-2 be multiplexed. The TES's used were fabricated of a molybdenum-copper bilayer and operate at 0.120 K. They have a

normal state resistance of 100 $m\Omega$ and alpha of 300 [2]. Figure 1.6 shows the differences in thermometry from SCUBA to SCUBA-2 [2]. SCUBA and now SCUBA-2, which is beginning to operate, allow for the study of galaxy formation and evolution.

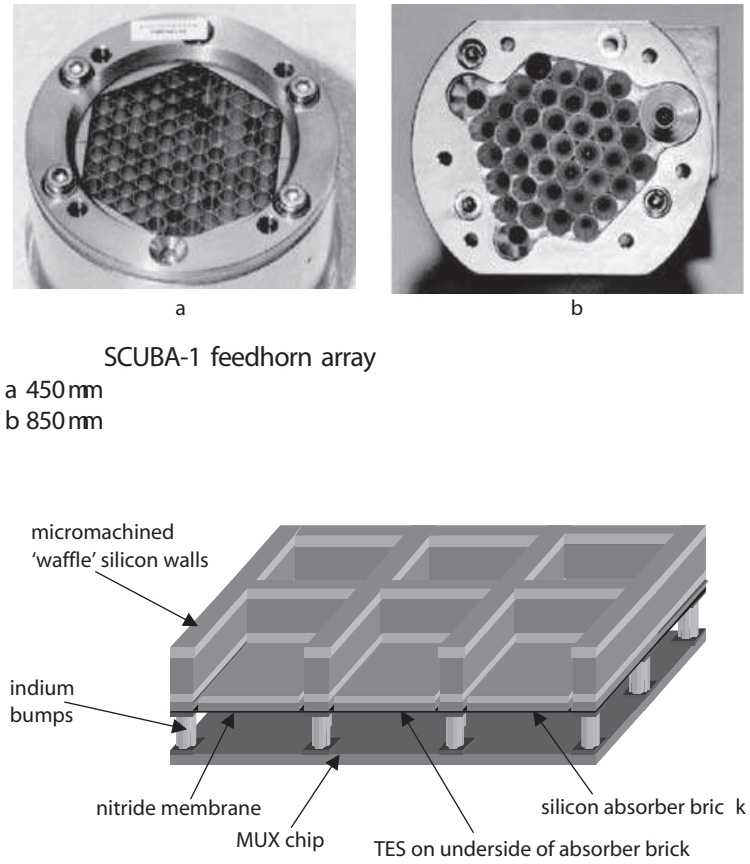

Figure 1.5: SCUBA-2 fabrication schematic view of hybridized detector and MUX chip [2].

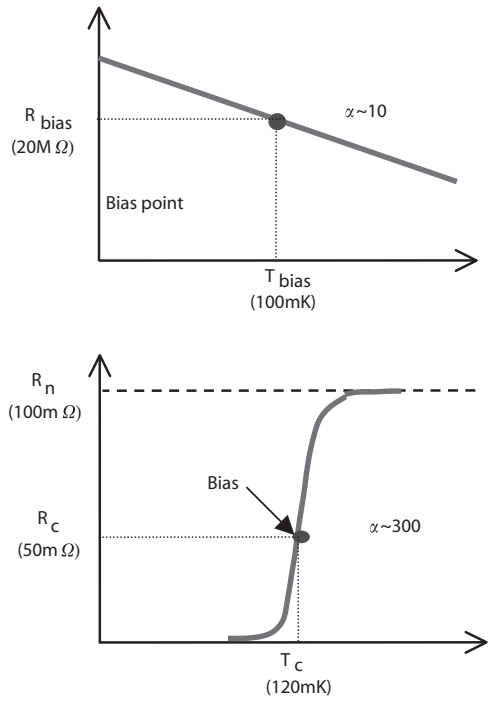

Figure 1.6: Comparison of detector technology in (a) SCUBA and (b) SCUBA-2. The slopes in these figures highlight the sensitivity of the devices [2].

1.8 Overview of Thesis

Following this introduction to TES's, Chapter 2 will discuss the uses of TES's in condensed matter physics followed by fabrication procedures and some issues encountered in Chapter 3. The experimental setup, including the low temperature apparatus used is presented in Chapter 4. The TES fabrication and characterization results are presented in Chapter 5. Chapter 6 switches focus to utilizing a TES in the measurement of the latent heat of a superconducting transition, followed by the results of those experiments in Chapter 7. Final discussion and concluding remarks end the thesis in Chapter 8. Appendices include a brief overview of ^3He fridge procedures and an overview of the TES collection at the University of Waterloo, presented in an easy reference format for further work.

Chapter 2

Using TES's in Condensed Matter Physics

2.1 Latent Heat Measurements

Latent heat is the heat absorbed or released during a first order phase change. The latent heat of a superconducting transition is the heat absorbed or released during the transition from the superconducting to normal phase of a type I superconductor.

A phase transition is classified into one of two types, first order or second order. In both types, the specific heat of the material undergoes a change. Latent heat is only observed in a first order phase transition. At zero magnetic field, the transition from normal to superconducting is second order [4]. One may be convinced of this by noting that the latent heat (Equation 2.1) is proportional to the field, which in this case is zero. Phase transitions below T_C (caused by exceeding the critical field) result in both a change in specific heat and an observable latent heat which indicates a first order phase transition.

$$L_H = \frac{B_0^2 * V * [1 - (T/T_C(B))^2] * (T/T_C(B))^2}{2 * \pi * \mu_0} [20] \tag{2.1}$$

Where L_H is the latent heat and $B_C(0)$ is the critical magnetic field at zero temperature. Classic latent heat measurements are performed by applying energy at a constant rate and graphing the temperature versus time. As the phase changes from one state to another, there is a plateau in temperature corresponding to the latent heat being absorbed or expelled. Classic measurements of latent heat are very large, for example, the latent heat of fusion of water is 6000 J/mol, compared to expected latent heat of superconducting transitions shown in Chapter 6 on the order of μJ/mol. External noise interference can make the latent heat much harder to detect. It is essential that one uses a thermometer with appropriate energy sensitivity for the expected latent heat. Measuring the latent heat of a superconducting transition requires a different techniques than classic methods. In an experiment by Ewert [20], superconductivity was broken adiabatically with an overcritical magnetic field, resulting in an observable latent heat as well as a change in specific heat.

Keesom and Van Laer [3] had the novel idea to measure the latent heat of the transition from the superconducting to normal state by applying a magnetic field above the critical field at constant temperature. A tin sample was cooled in zero field and then, once below the T_C, the temperature was held constant and the magnetic field was applied at a slowly increasing level. Once a decrease in temperature was noticed, heat was continually added from a heater to balance the cooling that was a result of the phase transition. This kept the experiment at a constant temperature. When the phase transition was complete, the cooling from the magnetic field could no longer compete with the applied current from the heater. The amount of time that constant heating was applied was directly related to how much energy was absorbed during the transition. The maximum latent heat measured was approximately 0.0013 cal = 0.005439 joules. The latent heat results are shown in Figure 2.1 [3]. In this experiment [3], emphasis was placed on ramping the magnetic field slowly, in order to reduce eddy current heating which would act to cancel the latent heat. Eddy current heating occurs at the surface of a normal metal when there is a change in applied magnetic field. In this case eddy currents were not an issue until superconductivity was

destroyed with the applied field. Then the material is normal and eddy currents are able to form. To make sure that the only heat observed is from the latent heat of transition, it is important to remove the heating due to eddy currents. Simple changes in the shape (and the orientation in regards to the magnetic field lines) can reduce eddy currents in the sample. A sphere which has a much larger surface area than a thin needle of the same mass and thus more room for eddy currents to form, is a poor sample geometry.

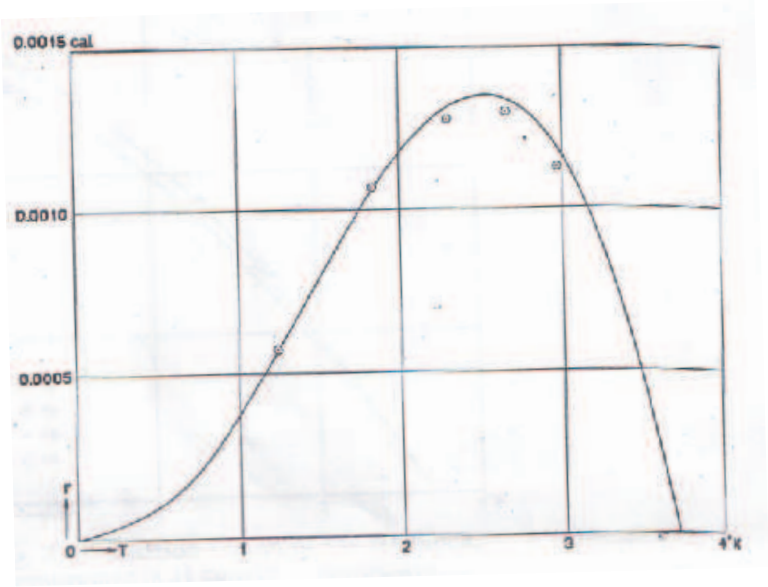

Figure 2.1: Keesom and Van Laer's atomic latent heat of tin results [3].

In quasi-adiabatic latent heat experiments, the total entropy remains constant. As the superconductivity is destroyed by magnetic field at constant temperature, there is absorption of heat as the cooper pairs are broken. In order to conserve entropy, the heat absorbed by the cooper pairs is released by the phonons and a cooling is observed during this experiment.

2.2 Cobalt Thermometry

Cobalt thermometers utilize the emission of γ-rays from a radioactive nucleus. Nuclear orientation thermometry is a primary thermometric method and is often used as a calibration tool. The cobalt thermometer is limited to a temperature range from a few mK to about 40 mK [21]. Although a narrow temperature range, this is a very useful and important range for extending the calibration of commercially available resistance thermometers. Also this is the range at which resistance thermometers become very sensitive to self heating and noise pickup. The Cobalt thermometer is immune to such noise.

The radioactive nuclei must all be oriented in the same direction in order to detect the anisotropy of the emitted γ-ray intensity. Cobalt is a very well understood, characterized material and the γ-ray intensity is well known as a function of temperature. Traditional cobalt thermometers consist of a nuclear source and a detector. The detector must point in the direction where the change of the γ-ray intensity is a maximum as a function of temperature. The detector is set up on the outside of the cryostat and since these two components are separate, each use requires good alignment for accuracy [21].

Utilizing a TES for this thermometer, a self contained system could be made. The TES could be mounted permanently aligned with the cobalt as one unit, improving reproducibility of results from one cool down to the next, as alignment is only required initially and will also make this thermometer much easier to use.

2.3 LC Resonator Tank Circuit Readout

A tank circuit has been developed in our lab for a single electron transistor (SET) readout. The speed of an SET was increased and the 1/f noise dependence was eliminated by using this circuit. This is currently being developed within our group. Similar results are anticipated for TES's.

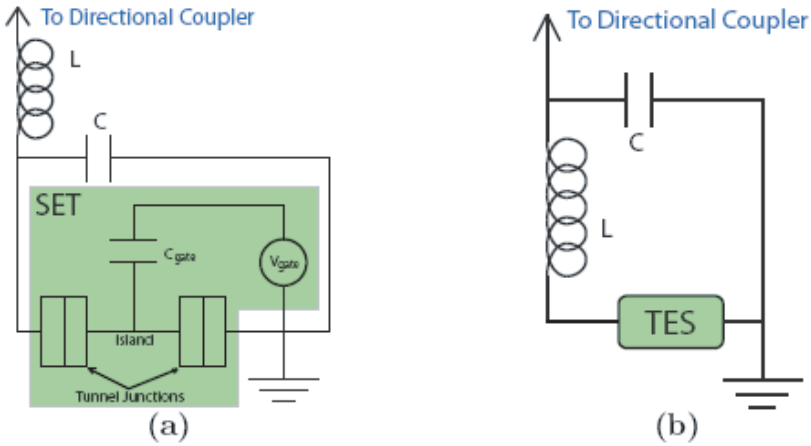

Figure 2.2: *a*) RF-SET tank circuit. *b*) TES tank circuit, with the order of L and C interchanged for appropriate impedance transforming.

A tank circuit is a very sensitive, high speed readout system. The circuit contains an inductor ('L'), a capacitor ('C') and a resistor ('R'). The existing circuit must be slightly modified, adjusted from reading out an SET with high resistance to a TES with low resistance. The two circuit configurations can be seen in Figure 2.2 [22]. The electronic components are selected for the final configuration and must be characterized to ensure optimal performance of the entire system.

A tank circuit works by measuring the change in damping of the resonant circuit caused by change of resistance, instead of measuring the changes in current through the device directly. The electronic readout measures this change in damping as the change in reflected power from the tank circuit when an incident carrier signal is applied. Impedance matching at the boundary between components determines how electromagnetic waves propagating through the circuit will be reflected or absorbed at that boundary.

Chapter 3

Fabrication

The TES's were lithographically patterned on a silicon wafer with a thin layer of photo resist of thickness approximately $0.7 - 2.1\ \mu m$. After exposing the resist through a mask, two metals were rf sputtered. Final lift-off, which consists of removing all unwanted metal and photo resist, produces a thin bi-layered metal. This procedure is shown in Figure 3.1. A sketch and photo of the final stage TES is shown in Figure 3.2. The full fabrication procedure and details of the equipment used can be found in Section 3.1. The mask was fabricated by Applied Image Group with a variety of widths such that in one fabrication many TES's were made with exactly the same parameters with the exception of width. Figure 3.3 shows the mask layout.

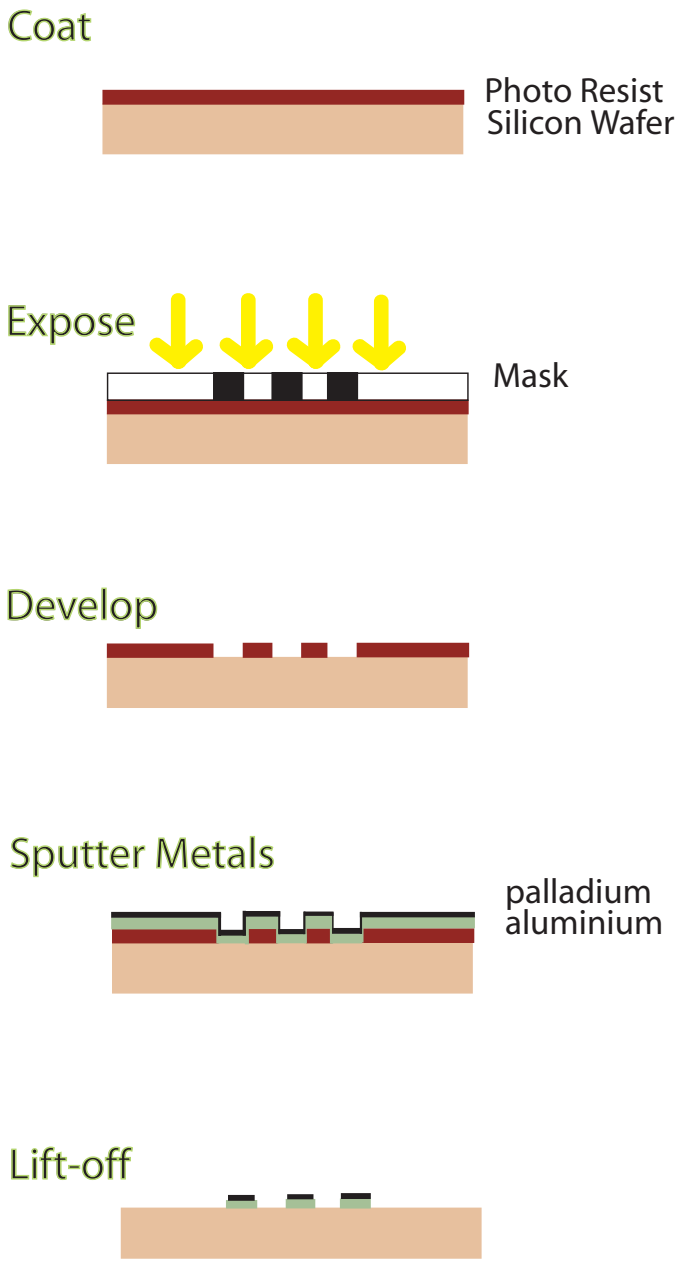

Figure 3.1: Photolithographic lift-off procedure.

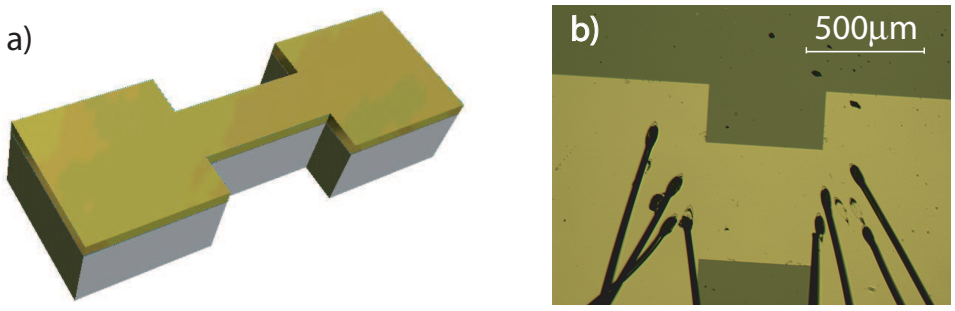

Figure 3.2: TES geometry. a) Exaggerated side view of bi-layer metals. b) Top view of the TES on silicon wafer with eight wirebonds.

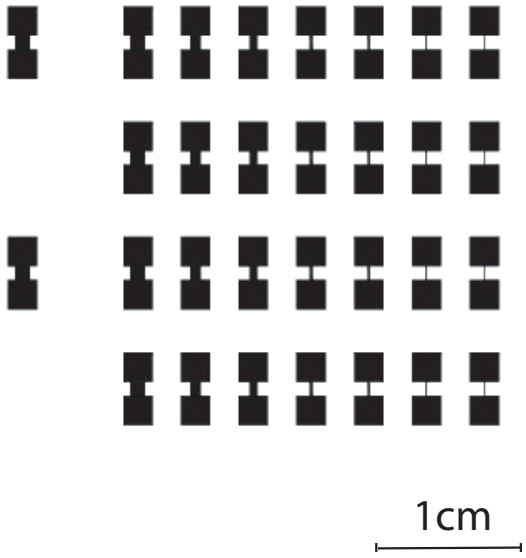

Figure 3.3: A section of the mask showing different widths (500, 350, 240, 100, 50, 20, 10 μm) and two additional 500 μm on the far left. All Devices have 500 μm distance between contact pads.

3.1 Procedure and Equipment Used

Devices were fabricated using negative photo resist NR9-1000PY from Futurrex Inc. that was spun to a thickness of approximately $0.7 - 2.1\ \mu m$ on clean two-inch Silicon wafers purchased from Virginia Semiconductor Inc. (silicon wafer specifications can be found in Appendix A) using a Headway Research Inc. Model PWM32 Spinner.

Spinner Recipe:
Step 1 : 5 seconds, 500 rpm
Step 2 : 45 seconds, 2300 rpm
Step 3 : 1 second, 0 rpm

The wafers were soft baked at 150 °C for 60 seconds on a metal sheet in an oven. This was necessary to remove any solvents and solidify the photo resist to prepare it for exposure. The wafer was diced using a diamond scribe.

A Karl Suss MJB 3HP Mask Aligner was used with a chrome plated glass mask made by Applied Images. The wafer was exposed with $350 - 500\ nm$ wavelength light for 20 seconds, with an intensity of 10.42 mW/cm^2.

The wafer was hard baked at 100 °C for 60 seconds on a metal sheet in a toaster oven. This aides the exposure and allows the photo resist to be developed. In order to complete the patterning process the wafer was developed with Futurrex, Inc. RD6 developer for ten seconds, followed by rinsing in deionized water. Rinsing ensured no further development occurred as well as to removed resist developer or resist residue. The wafer was then blow dried.

A Leybold Heracus Turbotronik NK450 sputtering system was used to make the bi-layer structure. Sputtering was done in an evacuated chamber at a pressure of $10^{-6} - 10^{-7}\ mbar$. Inert argon gas flooded the chamber at pressures of $1.3 * 10^{-2}\ mbar$. A DC potential of 800 V was set up between the target and the stage where the wafer was placed. The cathode current was 16 mA and high tension voltage 22% 5 $kV = 1.1\ kV$. Atoms in the

aluminium (or palladium) target were ejected due to ion bombardment from the argon gas. The ejected atoms formed a thin film on the silicon substrate. The bi-layer was created by first sputtering aluminium for two minutes at 800 V which corresponds to a thickness of approximately 20 nm and then waiting the same amount of time to let the wafer cool. Palladium was then sputtered for 20 seconds also at 800 V which corresponds to a thickness of approximately ten nm. Results from the rough calibration of aluminium sputtering rates can be seen in Figure 3.4. Eliminating one extreme data point, error of $\pm$ 5 nm is the maximum deviation, and there appears to be less error associated with a lower flow rate, with argon pressure approximately $1.3 * 10^{-2}$ $mbar$. It is unknown why this is the case. Reproducibility improves when sputtering two metals one after the other instead of exposing to air or even another gas. [17]

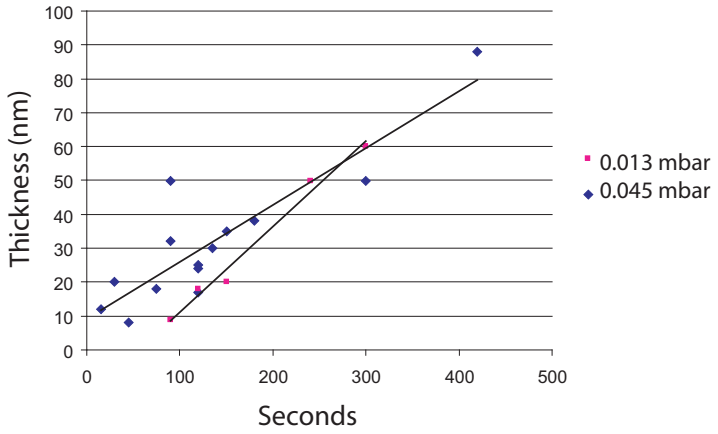

Figure 3.4: Calibrating sputtering system for aluminium target.

The remaining photo resist and unwanted sputtered metal was removed using acetone, then rinsing with deionized water and blowing dry. The wafer was cut again to size.

Film thickness was measured with a Veeco Dektek 6M Stylus Profiler. The devices were mounted and wirebond connections were made to the electrical pads with a K&S Model 4526 Wirebonder. Typical wirebond contacts are shown in Figure 3.2b.

3.2 Notes

- New whole wafers are best when spinning photo resist. Cutting wafers before spinning results in uneven resist thickness. Attempts to clean and reuse wafers were not successful and the second attempts were not useable.
- Soft and hard baking and developing times are the most prone to human error, but do not appear to have much influence on the final product.
- Fabrication from start to finish was done in as short a time as possible to prevent any contamination, oxidation, aging or additional light exposure from occurring.
- Devices were clamped to heat sinking plates to improve reproducibility of film thickness and quality. This was initially not done.
- The chamber was evacuated to a pressure of $10^{-6} - 10^{-7} mbar$. An assumption is that this can change the sputtering quality as the pressure determines the amount of contaminants in the chamber.

- The bi-layer is sputtered one metal and then the other. Heating occurs when sputtering and to limit diffusion between the two hot metals an amount of cool down time is required. The temperature reached when sputtering is not known, and the amount of time required for cool down is also not known. Al-Pd alloy forms at 540 °C [1] and photo resist melts above 150 °C. So it is important to keep the temperature below these limits while sputtering. Other groups wait until the substrate has reached room temperature between depositions to minimize inter-diffusion of the two materials [11]. Aluminium was sputtered first in all cases such that an aluminium oxide barrier does not form on the surface, in addition to the fact that wire-bonding is easier on palladium surfaces compared to aluminium (due to the oxide layer).

- The sputtering process is done manually and there is an error of $\pm 10V$ associated with it. This corresponds to the error shown in Figure 3.4.

- The sputtering time is controlled by a hand operated knob and stop watch, this corresponds to an error of approximately two seconds. This error is less than the error associated with the voltage accuracy.

Chapter 4

Experimental Setup

4.1 Sensors

The sensor chosen for further use in latent heat of superconducting transition experiments (which are detailed in Chapter 6 and 7) was ID:N29C-b . This TES was fabricated on the same wafer as ID:N29C-a with identical fabrication procedures, including simultaneous deposition. An assumption was made that since the two devices were fabricated together they would have very similar if not identical parameters. The final characterization was very different than what was expected. Measured parameters are reported in Table 4.1.

Table 4.1: TES ID N29C comparison.

	N29C-a	N29C-b
R_N	15 Ω	35 Ω
T_C	650 mK	700 mK
transition width	5 mK	330 mK
α	500	5

These two TES's were fabricated on the same chip approximately one and a half centimeters apart and the wafer was cut at the end of the fabrication procedure. N29C-a was characterized attached to a copper sheet with GE varnish. The copper was heat sunk with a screw to make good thermal contact with the stage of the ^{3}He fridge (see details in Chapter 4.2). Electrical contacts were made with aluminium wire bonds. This is the procedure with which the majority of TES's in this thesis were characterized. However, N29C-b was not characterized using the same methods as it was set up to be used in the latent heat experiment. N29C-b was GE varnished onto a second piece of silicon which was weakly connected to a copper stage via a platinum-tungsten wire. A second difference is that electrical contacts were made with tiny niobium-titanium filaments connected with 4110 Epo-Tek silver epoxy. This setup is detailed in Section 6.2. Although these parameters were not what was expected, this sensor was found acceptable to continue with the latent heat of superconducting transition experiment.

4.2 Low Temperature Apparatus - ^{3}He Refrigerator

The experiments described in this thesis were performed on a Janis ^{3}He Cryostat. Procedures for using this cryostat can be found in Appendix B. The cryostat is shown in Figure 4.1 with major parts highlighted.

The ^{3}He fridge is used inside a vacuum can which is immersed in liquid ^{4}He. The ^{3}He pot is connected by a stainless steel tube, through a 1K pot, to a charcoal adsorption pump and to an external storage bottle. Initially the charcoal is heated above 40 K to evaporate the ^{3}He which condenses on the 1K pot and drips into the ^{3}He pot. Once the condensation is complete, the charcoal is cooled and acts as a pump, cooling the fridge to a base temperature of less than 250 mK [23].

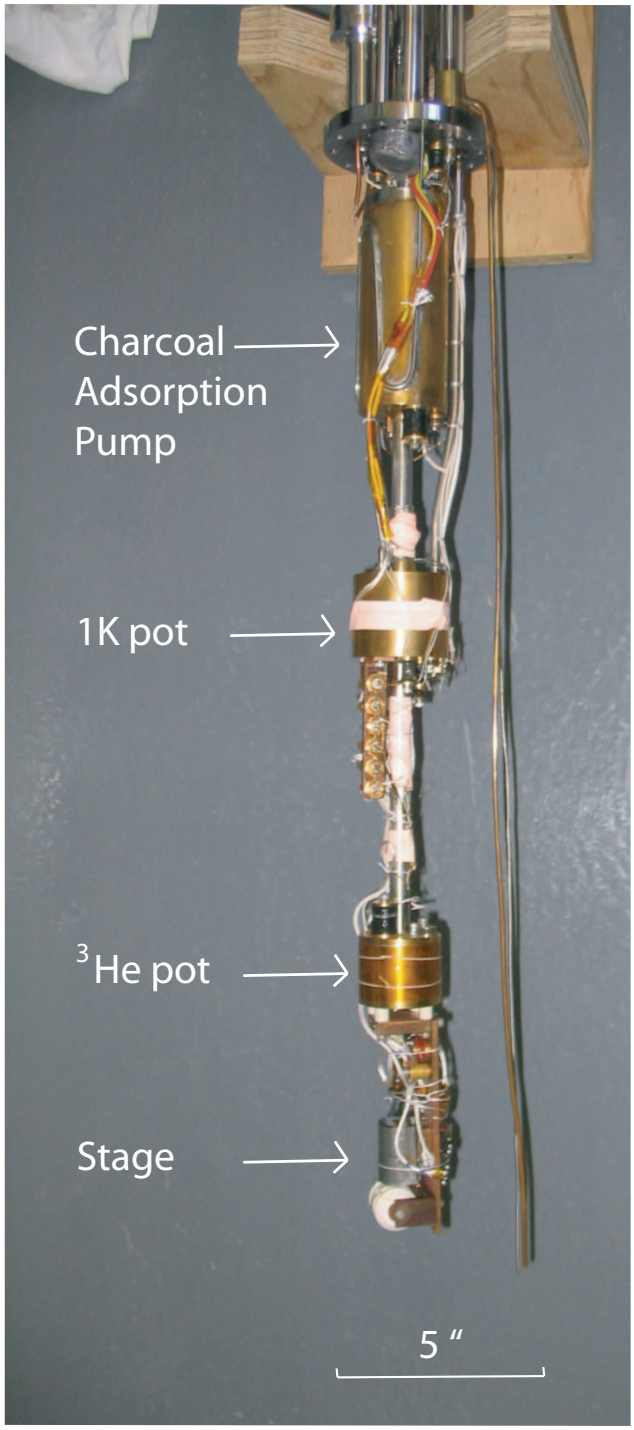

Figure 4.1: ^{3}He Refrigerator.

4.3 Electronics

To measure a low noise voltage differential, a lock-in amplifier is the preferred tool. It applies an AC voltage excitation that can be converted to a current excitation using a large resistor in series ('current limiting resistor'). The lock-in used in these experiments is a Stanford Research Systems, model SRS-830. It is a two phase system, measuring the voltage difference across two input leads, which are in and out of phase with the excitation. This technique isolates the signal from other noise sources such as 60 Hz pickup and low frequency drifts due to thermocouple effects in the leads. Measurements in this thesis were done at 1028.6 Hz which was chosen for reasonable time constants and far from 60 Hz harmonics. This AC technique also has the advantage of being able to incorporate a low noise transformer setup, such as the Princeton Applied Research 1900 (PAR-1900) used in this work. An ideal differential voltage meter would have infinite resistance between the inputs, which draws no current. The input impedance of the SRS-830 lock-in is 1 $M\Omega$, which is very convenient as it has a noise at 1 kHz of 5 $\frac{nV}{\sqrt{Hz}}$ when measuring a resistance less than 1 $k\Omega$. A simple example of a four terminal current biased readout is shown in Figure 4.2. From this schematic, you see the $1M\Omega$ input impedance of the lock-in means that very little current will flow through the lead resistance. 1 $M\Omega = Z_{input} >> R_{sample} + R_{lead3} + R_{lead4}$. This makes the voltage drop across these leads insignificant and $V_1 - V_2 = V_3 - V_4$. Virtually all of the supplied current (voltage output from lock-in / current limiting resistor) passes through R_{sample}. The voltage drops across R_{lead3} and R_{lead4} are not important.

When measuring a much smaller resistance such as $R < 1\ \Omega$, the lock-in can be used with a transformer, such as the PAR-1900 transformer with 100x voltage gain, which has an input impedance of 600 Ω at a frequency of $200Hz$. The noise at the input is likely due to Johnson noise of the windings and is about 0.5 $\frac{nV}{\sqrt{Hz}}$. The gain of the transformer is 100 and the noise of 0.5 $\frac{nV}{\sqrt{Hz}}$ at the input is referred to as 50 $\frac{nV}{\sqrt{Hz}}$ at the output, making the noise of the SRS-830 lock-in (5 $\frac{nV}{\sqrt{Hz}}$) insignificant. It is important to use low resistance leads as the input impedance is much lower than the lock-in amplifier ($Z_{input} = 600\ \Omega$). The schematic for this setup can be seen in Figure 4.3. The third

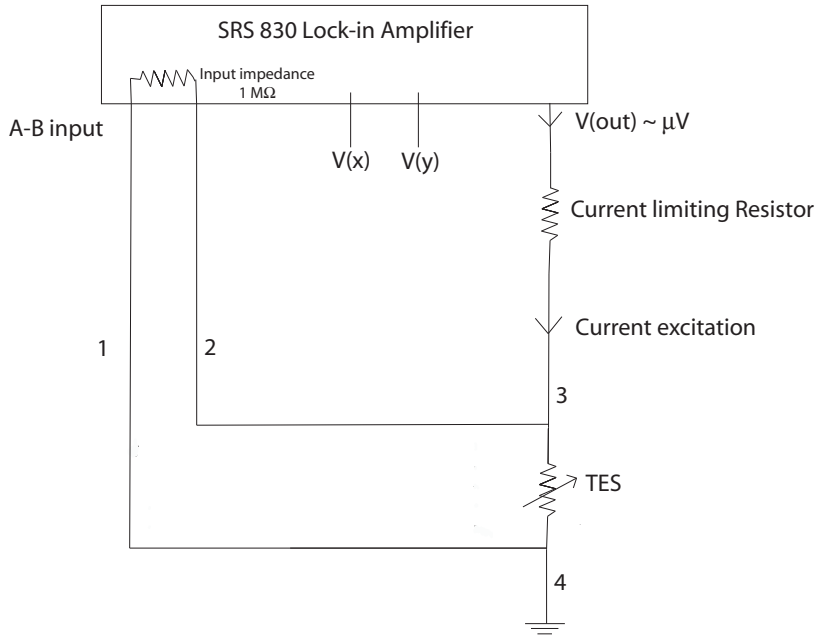

Figure 4.2: Four terminal readout schematic.

improvement is to use a cryogenic transformer. This has the advantage of having a lower noise. The input impedance is 10 Ω with a gain of 30. Since this is a low temperature device, the leads (denoted '3' and '4' in Figure 4.3 used are superconducting and so the additional lead resistance is not an issue. A transformer is a passive device as it cannot add energy. The power at the input ($\frac{V_{in}^2}{Z_{in}}$) must equal the power at the output ($\frac{V_{out}^2}{Z_{out}}$). Since there is a 30 times gain ($V_{out} = 30\ V_{in}$), there is an increase of output impedance ($Z_{out} = (30)^2\ Z_{in}$). This schematic is the same as the one shown in Figure 4.3 with the modification that there is no lead resistance between the sample and the amplifier (leads '3' and '4'), as superconducting leads are used.

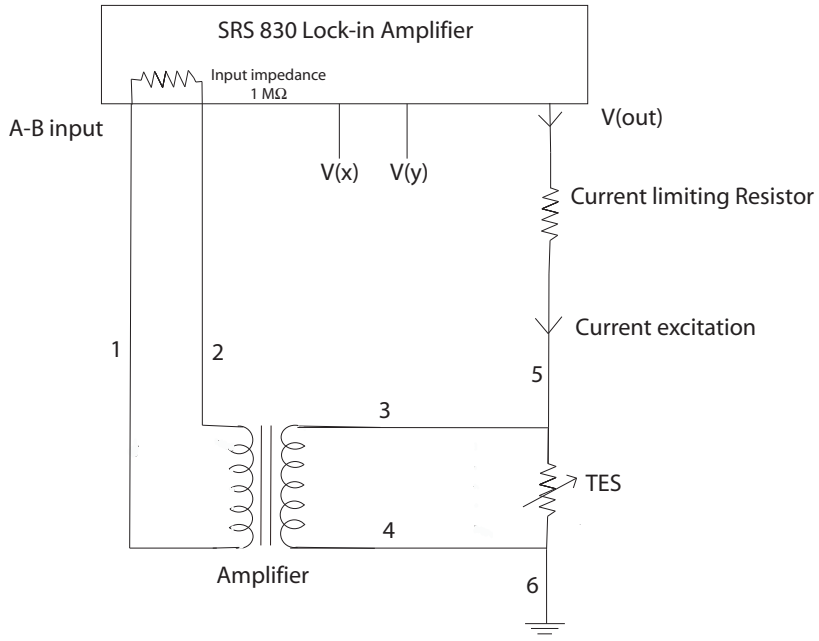

Figure 4.3: Four terminal readout schematic with amplifier.

4.4 Readout methods

Following the brief outline of readout methods in Section 1.5.1, this Section calculates and compares the sensitivity for the two methods: 1) current biased four wire technique used to characterize the resistance-temperature correlation, alpha and width of the sensors and 2) quasi-voltage biasing negative electrothermal feedback (ETF), which is the anticipated method to be used in the latent heat of superconducting transition experiment.

4.4.1 Current Biasing Four Wire Measurement

Calculating the sensitivity of a current biased TES Readout Circuit

The wiring schematic for a TES output is shown in Figure 4.3 with a PAR-1900 low noise transformer as the amplifier. To determine the energy sensitivity of the TES readout circuit (noise floor of the readout, not the intrinsic noise sensitivity of the TES), one must work backwards from the noisiest piece of electronics, in our case the SRS-830 lock-in amplifier which has an internal noise of 5 $\frac{nV}{\sqrt{Hz}}$. Since we have a gain of 100 from a room temperature low noise transformer (PAR-1900), we can divide the lock-in noise by 100 to determine that the maximum noise contribution from the lock-in is 0.05 $\frac{nV}{\sqrt{Hz}}$. The noise from the transformer is 0.5 $\frac{nV}{\sqrt{Hz}}$ The total noise of the system is added in quadrature: $\delta V = \sqrt{(\delta V_{PAR1900})^2 + (\delta V_{Lock-in})^2}$. This results in a total noise observed by the TES to be 0.502 $\frac{nV}{\sqrt{Hz}}$. Typically resistance versus temperature data is recorded for a TES, which can be quickly converted to voltage versus temperature, yielding a typical slope of $1V/K$. By multiplying our internal noise by the slope, we can determine the temperature noise to be 0.502 $\frac{nV}{\sqrt{Hz}} * 1\ K/V = 0.502\ \frac{K}{\sqrt{Hz}}$. Finally we must determine the energy sensitivity, which is the standard noise parameter used for comparison. The thermal weak link (further information about thermal links will be discussed in Section 7.2) used in the experiment converts heat into a temperature change. For example, 25 nW will raise the temperature 1 Kelvin. By multiplying this by the temperature sensitivity, the energy sensitivity of the readout noise floor is determined: $12.55 * 10^{-9} \frac{W}{\sqrt{Hz}}$. This sensitivity will change depending on the amplifier, and if any noisier electronics are added to the circuit. It is important to check if a preamplifier, filter etc has a higher noise than the lock-in amplifier input.

4.4.2 Quasi-Voltage Biased Negative Electro-Thermal Feedback

A voltage biased sensor results in a better readout system as it prevents run away problems. We have devised a quasi-voltage biased circuit set up to allow negative ETF, shown in Figure 4.4. The advantage of this is that we can work with the convenient voltage amplifier transformer, instead of a SQUID, as a current meter. A SQUID is more complicated to implement, sensitive to electromagnetic noise and may be destroyed by electrostatic discharge. It requires specialized control electronics which can increase the cost of the experiment. A SQUID is used in a voltage biased configuration for measuring the current as shown in Figure 4.5a, compared to the LTT circuit in Figure 4.5b. It is important that the resistor in this circuit is smaller than the resistance of the TES, so that when the TES resistance changes, the current running through the resistor changes and the current measured also changes.

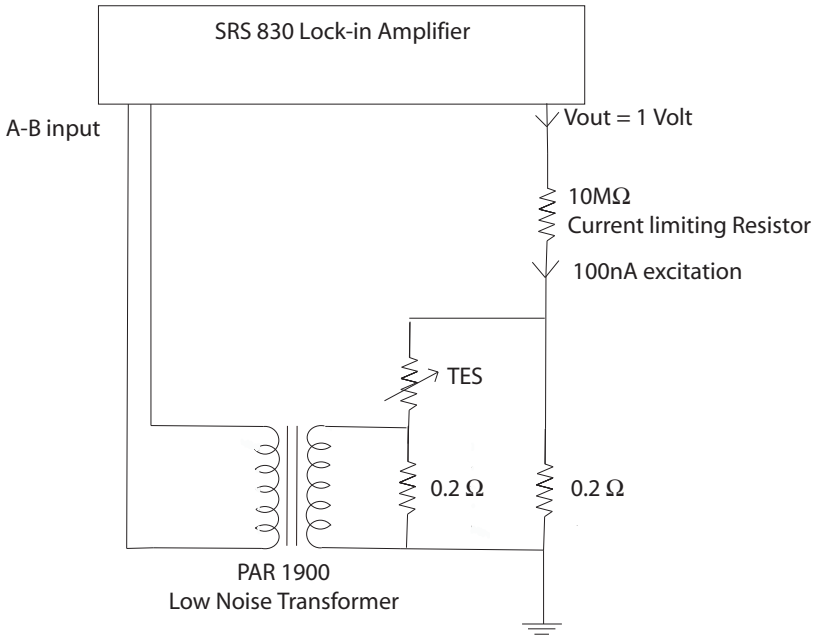

Figure 4.4: Schematic of Quasi-Voltage biased readout with a Low Temperature Transformer.

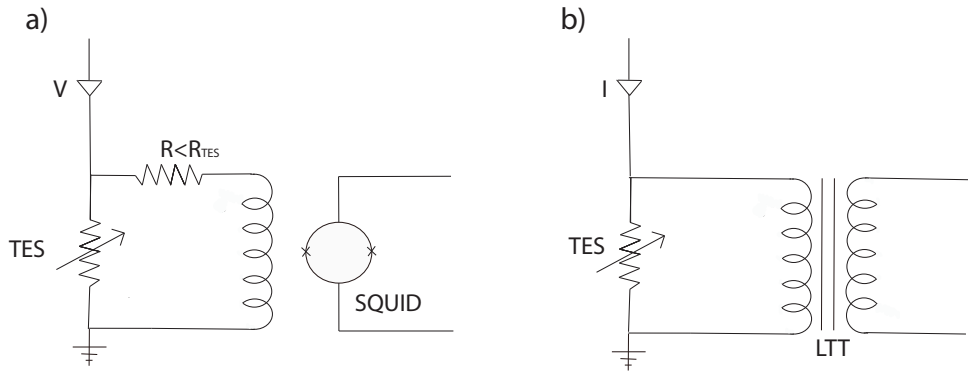

Figure 4.5: Comparing TES readout schemes; a) SQUID, b) Low Temperature Transformer.

In the circuit shown in Figure 4.4, there is a shunt resistor of 0.2 Ω, parallel to the TES. Since this resistance is much smaller than the resistance of the TES (ranges from 0 to 25 Ω) most of the current will run through this shunt resistor defining the constant voltage across the TES. This set-up is deemed quasi-voltage biased as any small change in TES resistance due to temperature change will change the voltage slightly.

The TES is readout using the LTT (cryogenic transformer) (30x gain) instead of the 100x gain from the room temperature low noise transformer (PAR 1900). The low temperature (in comparison to room temperature amplifiers) allows a very low noise contribution to the measurement. Due to the quasi-voltage biased setup, the input to the LTT is a 0.2 Ω resistor and not the TES. The transition goes from zero resistance at high temperatures to full resistance at low temperatures. The resistance of the TES is then determined. The TES output can be seen in Figure 4.6. The figure shows the LTT output and the calculated TES output. The upper graph shows the alpha parameter as it changes across the transition.

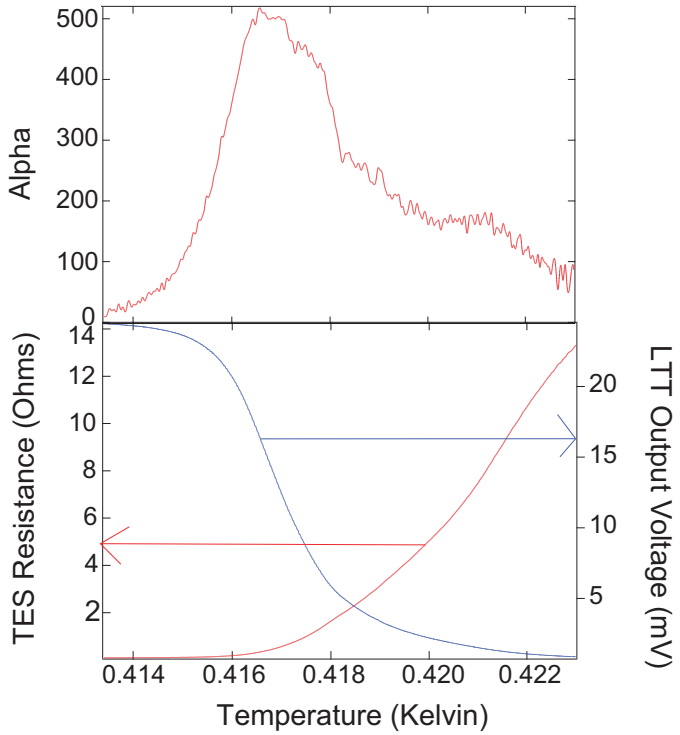

Figure 4.6: Low temperature transformer output, TES resistance and alpha as a function of temperature.

Calculating the sensitivity of a voltage biased TES Readout Circuit

Using the circuit shown in Figure 4.4 and referring to the method used in the four wire current biasing sensitivity calculations in Section 4.4.1, the sensitivity of the voltage biased TES readout can be calculated.

Using the LTT cryogenic transformer in place of the room temperature PAR-1900 transformer, the total noise seen by the TES is $\delta V = \sqrt{(\delta V_{LTT})^2 + (\delta V_{lock-in})^2}$ where δV_{LTT} is extremely small such that the noise of the lock-in amplifier is the primary noise contribution. This readout method is found to be more sensitive than the four-wire current biased method with the limitations being the electronics used.

4.4.3 Intrinsic Noise Sensitivity

The intrinsic noise of the TES is known as the thermal or Johnson noise and can be found from Equation 4.1

$$\Delta V = \sqrt{4\ k_B\ T\ R\ \Delta f} \tag{4.1}$$

where k_B is the Boltzmann constant, T is the temperature, R is the resistance and Δf is the bandwidth. For the midway point of the TES in Figure 4.6: 7 Ω, 417 mK and $\Delta f = \frac{5}{64\tau}$ where τ is the lock-in time constant results in a Johnson noise of $3.55 * 10^{-12}\ V$ per reading. The bandwidth is determined from the lock-in parameters. This is on the order of 1000 times smaller than the intrinsic noise of the lock-in amplifier and does not play a significant role in the sensitivity calculations found in Sections 4.4.1 and 4.4.2.

Chapter 5

TES Results and Discussion

The results of working TES's are presented in this Chapter. 'Working' is defined as a device with transitions observed, not necessarily that it has ideal parameters for further applications. TES's in our lab have been fabricated using aluminium and palladium bi-layers. Aluminium has a $T_c = 1.2\ K$, taking advantage of the proximity effect, the aim was to have working TES's in the range from 10 mK to 1 K. From the definition of electrical resistance, it is understood that as the physical width of the TES is increased, the resistance is decreased ($R = \rho l/A$, where ρ is the resistivity, l is the length and A is the cross sectional area). This is why different mask widths were chosen. Small resistances can be beneficial, especially if working with SQUIDS where a small resistance is preferred, as was discussed in Section 4.4.4. We have anticipated and verified that with increasing width, the alpha value also increases. This can be seen by comparing the characteristics of TES ID's Ap11L-a and -b. It is expected this is due to edge effects, as the width is increased, the edges become less significant as they are a smaller ratio of the whole device.

5.1 TES Characterization

All the TES's discussed in this thesis are characterized using a four wire current biased method. Constant current is applied to the TES and the corresponding voltage is recorded with a SRS 830 Lock-in Amplifier. While the voltage is being measured, the heat applied to the stage of the ^{3}He fridge is slowly lowered so that the full transition is documented.

TES results are shown in Table 5.1. The best TES (ID: JL15B) was anticipated to be used for a latent heat experiment. This device was connected by niobium-titanium filaments and connections were made with Epo-Tek H20E silver epoxy which was baked at 80 °C for 120 minutes. From the binary phase diagram in Figure 1.4, heating at this temperature should not have significantly effected the composition of the metals, but may have increased the rate of diffusion between materials. Plans to investigate this in a controlled manner were discussed but not performed. After this modification, the TES did not behave in the same pre-bake manner and the transition could no longer be found down to 300 mK. Future connections for other sensors were made using Epo-Tek 4110 silver epoxy which cures at room temperature with an inconvenient three day cure time, or with aluminium wire bonds to prevent further heat-related damage of devices.

5.2 Summary of Working Sensors

Over 92 aluminium-palladium TES's were fabricated and 28 of these were tested. Of those 28, 13 were found to function. Many devices were not tested or characterized due to fabrication issues including poor lift-off procedures, inadequate exposure and/or developing, unacceptable surface quality and cracked devices. Some models were cooled but not measured due to broken leads, poor contacts and broken wire bonds. Devices in which transitions did not occur above 300 mK were also discarded as they would require the use of a dilution refrigerator for characterization. Since experiments were planned to be performed on the ^{3}He fridge, a device with a T_C below the base temperature of the fridge (250 mK) was not useful. TES's were characterized by their resistance-temperature curves and the α parameter determined from those curves. Of the 13 devices studied, the T_C ranged from

0.295 K to 1.46 K with α ranging from 3 to 7000. Of these, one was selected for further use in latent heat of superconducting transition discussed in detail in Chapter 6 and 7. A detailed summary of each sensor is found in Appendix C.

The relationship between α and T_C, transition width and T_C and film thickness and T_C are shown in Figures 5.1, 5.2 and 5.3. No clear correlation can be found from these graphs. All working transitions are shown in Figure 5.4. This Figure easily compares sensors to each other, working temperature range and sensitivity.

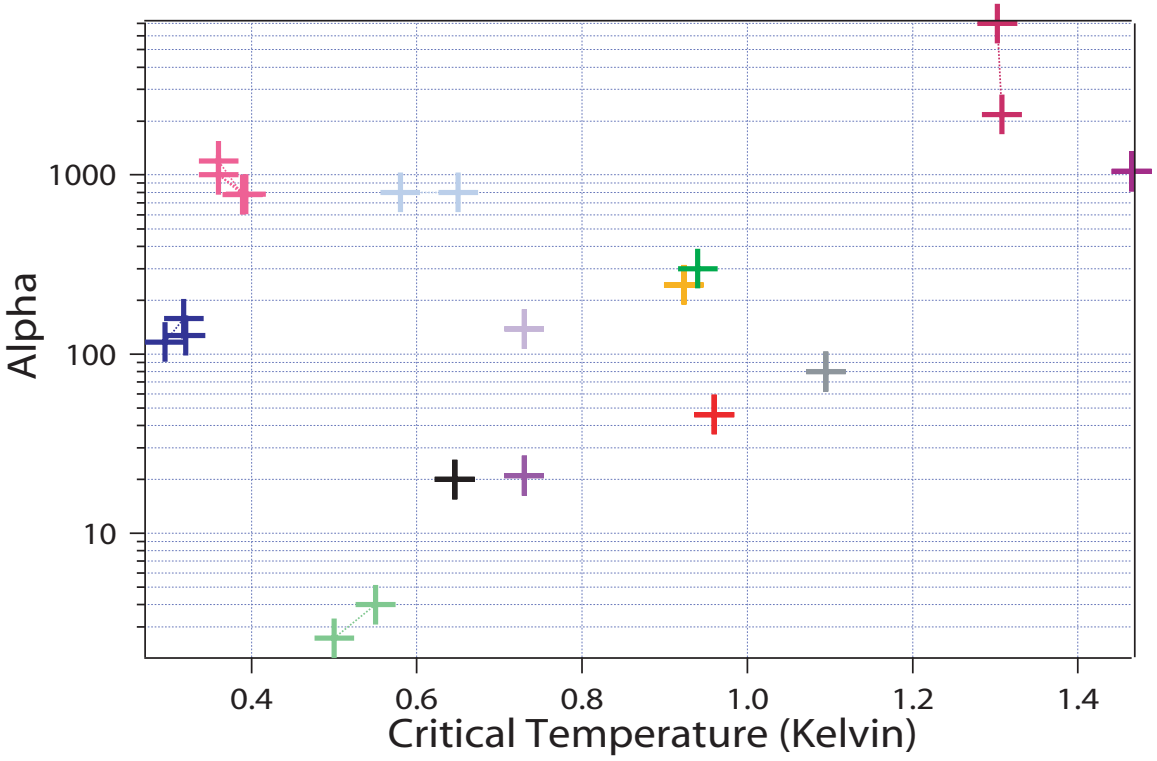

Figure 5.1: TES results highlighting correlation between transition temperature and alpha, lines between points indicate changing results for multiple cool downs.

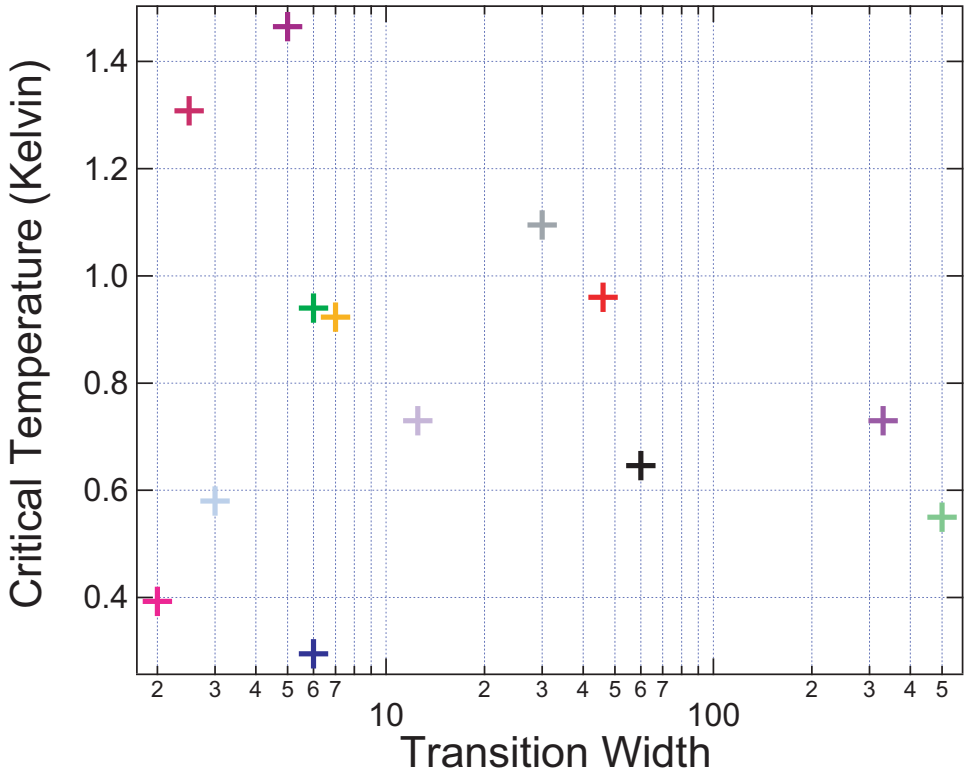

Figure 5.2: TES results highlighting correlation between transition temperature and transition width.

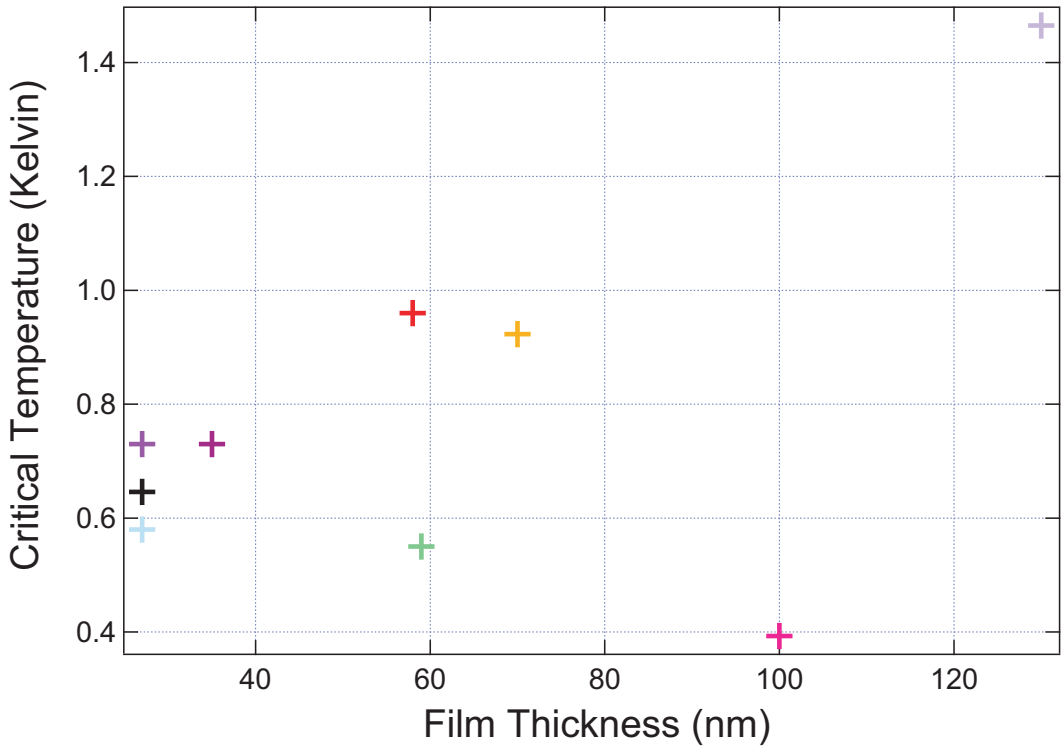

Figure 5.3: TES results highlighting correlation between transition temperature and film thickness.

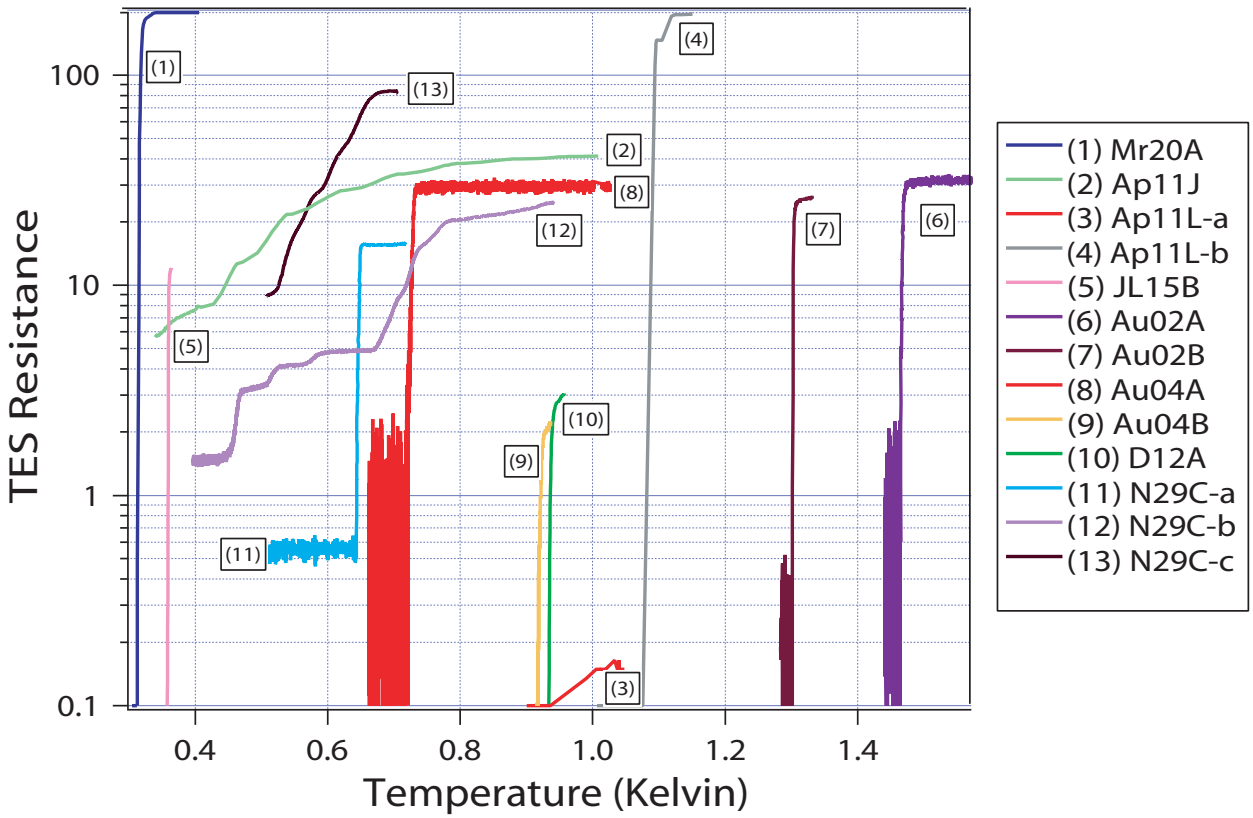

Figure 5.4: Collection of all measured TES transitions showing resistance-temperature characterizations.

Table 5.1: Summary of Working TES's

ID	Sputtering Information	Dimensions (μm)	Thickness ($\pm 5\ nm$)	Resistance (Ω)	T_c (K)	α	Transition Width (mK)
Mr20A	Al - 6min Pd - 1.5min	20 x 500		200	0.318	600	6
Ap11J	Al - 6min Pd - 1.5min	20 x 500	59	42 13	0.55 0.5	4 2.6	400 575
Ap11L-a	Al - 6min Pd - 30sec	20 x 500	58	243	0.96	46	46
Ap11L-b	Al - 6min Pd - 30sec	20 x 300		88	1.095	80	30
Jl15B	Al - 2min Pd - 20sec	500 x 500	100	16 14 16 12	0.393 0.360 0.389 0.360	783 1000 778 1200	2.3 1.8 3 1
Au02A	Al - 2min Pd - 10sec	500 x 500	130	36.2	1.4655	1047	5
Au02B	Al - 2min Pd - 10sec			22 22.2	1.308 1.3026	2179 7234	2.5 2.7
Au04A	Al - 2min Pd - 20sec	500 x 500	35	32.8	0.73	138	12.5
Au04B	Al - 2min Pd - 15sec	500 x 500	70	20	0.923	244	7
D12A5	Al - 2min Pd - 10sec	500 x 500		3.8	0.94	300	6
N29C-a	Al - 2min Pd - 20sec	500 x 500	27	15 15 15	0.580 0.65 0.649	800 800 500	3 3 5
N29C-b	Al - 2min Pd - 20sec	500 x 500	27	35	0.700	5	330
N29C-c	Al - 2min Pd - 20sec	100 x 500	27	82	0.646	20	60

Chapter 6

Latent Heat of Superconducting Transition

6.1 Motivation

Heavy fermion superconductors have differences from conventional BCS superconductors which are not completely understood. Work has been done on $CeCoIn_5$ [24], [25], [26], UPt_3 [27] and other heavy fermion systems [24], [25]. Detailed phase diagrams with multiple phase transitions have been constructed for the $CeRh_{1-x}Ir_xIn_5$ heavy fermion family of superconductors [25]. A double transition to the superconducting state in zero field has been seen routinely in UPt_3. Latent heat measurements, and the confirmation of first order phase transitions will be very important in heavy fermion superconductor theory field [25], [27], [28] as the existence of first order phase transitions could be confirmed.

6.2 Apparatus

Measurements of the latent heat of superconducting transition were performed by isolating a sample and a sensor and maintaining them at a constant temperature. The sample was then brought from the superconducting state to normal state with the application of an external magnetic field. The read out for this experiment is planned to be done using a quasi-voltage biased negative feedback circuit, which was discussed in detail in Section 4.4.2.

The experimental setup is shown in Figure 6.1. Consisting of a silicon beam suspended above a block of copper with thin fibers of dental floss held in place by superglue and GE varnish. The TES, superconducting sample and a ruthenium oxide thermometer (RuO_2) were mounted on the silicon beam and isolated from the copper by a platinum-tungsten thermal weak link. The copper was heat sunk to the ^{3}He Fridge stage. The zinc end of the silicon beam was placed inside a magnet while the TES and RuO_2 (mounted on the opposite end of the silicon) were enclosed in a lead shield to protect from stray magnetic fields. The TES and RuO_2 were wired with NbTi wire filaments and Epo-Tek 4110 room temperature curing silver epoxy. The platinum-tungsten weak link was connected with Epo-Tek H20E baked silver epoxy to the silicon and a screw clamp contact on the copper block. The superconducting sample used was an oblong piece of zinc weighing 22.4 mg.

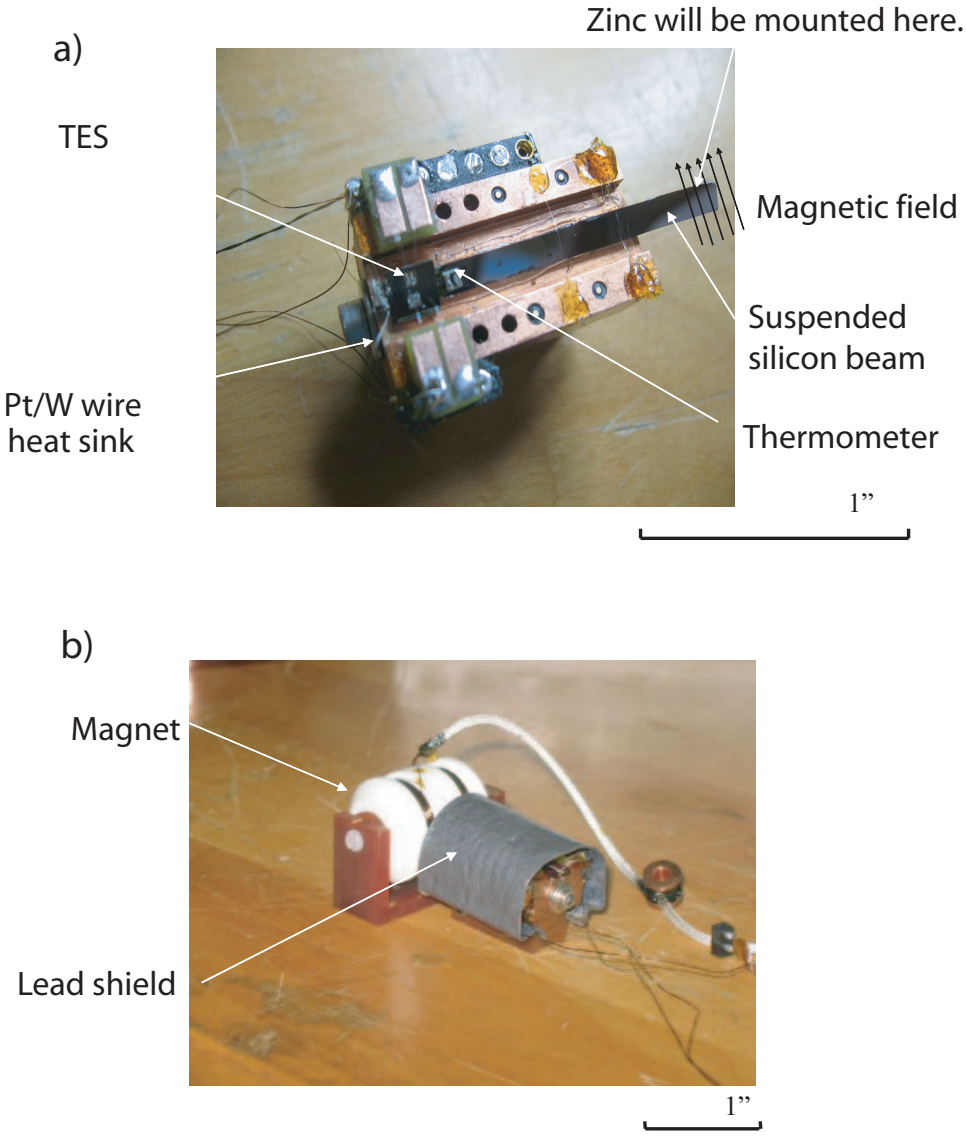

Figure 6.1: Latent Heat experimental setup. a) TES mounted on silicon beam suspended above copper block. b) Sample partially enclosed in lead shield and silicon beam with sample inserted into Helmholtz coils.

6.3 Magnet Properties

A Helmholtz coil was used in this experiment, made using monofilament NbTi/CuNi clad wire, 0.003 inches in diameter. Each coil has 700 turns and an average radius of 0.25 inches. A simple calculation can determine the current needed to achieve a certain field.

$$B = \frac{4}{5}^{3/2} \frac{\mu_0 n I}{R} \tag{6.1}$$

Where B is the attained field, μ_0 is the permeability of free space, n is the number of turns, I is the applied current and R is the coil radius. For our coil, one milliampere corresponds to one Gauss.

Using a narrow silicon beam, the zinc is mounted on one end and then placed inside the helmholtz coil to the area of uniform field. It is important that the sample is placed correctly as the area of uniform field is next to a low field region.

The nearly uniform magnetic field which is produced in the center of the coils is great for the experiment, but there is also a smaller magnetic field produced around the coils which the TES and GRT will see and potentially react to. The TES and $Ru0_2$ thermometer are more than one inch away from the coils center, they are calculated to see less than two Gauss (at the 40 Gauss required for the zinc to see the phase transition) and the GRT which is more than three inches away will see less than half a Gauss. Germanium resistors are known to have a field dependence and is very noticeable for large applied fields (kGauss) but an absence of sensitivity at these very low magnetic fields [29],[30].

6.4 Expected Results

As far as we know the latent heat of zinc has never been measured. Using thermodynamics [20], theoretical latent heat of superconducting transition are shown in Equations 6.2-6.7 and the known critical magnetic field at zero Kelvin and the known critical temperature at zero applied magnetic field, for zinc these values are 0.855 Kelvin and 53.4 Gauss. This is assuming there is no need for a demagnetization factor due to the shape of the sample used. The latent heat is shown as a function of temperature in Figure 6.2. This figure also shows the critical magnetic field of zinc as a function of temperature. From this graph we can determine if our magnet will be able to produce a large enough field and also if the TES and LTT readout will be sensitive enough to detect the expected latent heat. We plan to operate at 743 mK which corresponds to a latent heat of $6.1 * 10^{-6} \frac{J}{mol}$, requiring a magnetic field of 13.1 Gauss.

$$L_H = \frac{-VTH_C(T)}{4\pi} \frac{dH}{dT} \mu_O \tag{6.2}$$

$$H_C(T) = H_C(0)[1 - (T/T_c)^2] \tag{6.3}$$

$$\frac{dH_C(T)}{dT} = -2H_c(0) \frac{T}{{T_C}^2} \tag{6.4}$$

$$L_H = \frac{H_C^2 V[1 - (T/T_c)^2](T/T_c)^2}{2\pi} \tag{6.5}$$

$$B = \mu_0 H \tag{6.6}$$

$$L_H = \frac{B_0^2 V[1 - (T/T_c)^2](T/T_c)^2}{2\pi\mu_0} \tag{6.7}$$

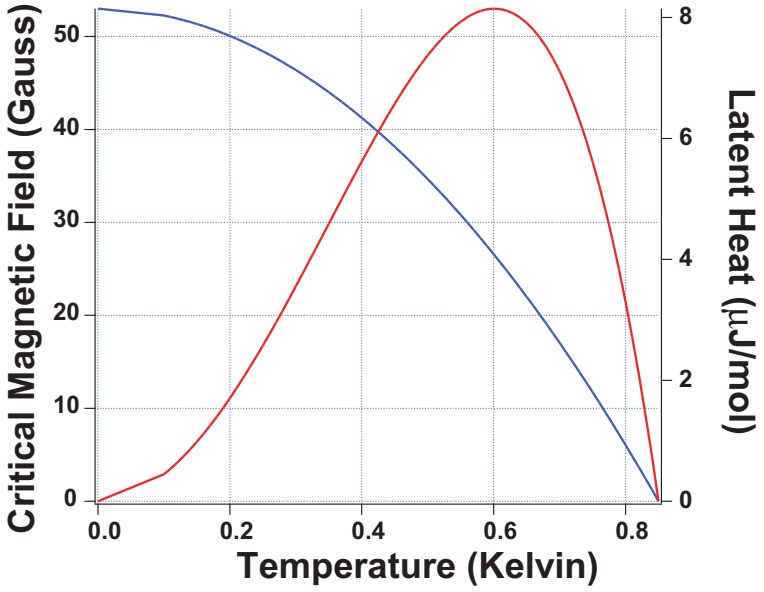

Figure 6.2: Calculated latent heat (red) and critical magnetic field (blue) versus temperature of zinc.

6.5 Sample Calculations

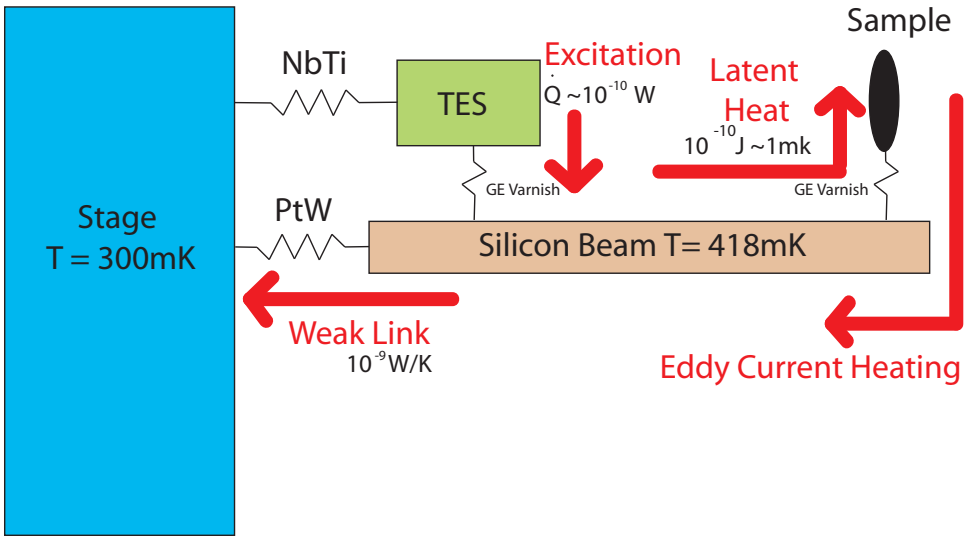

Figure 6.3: Heat Flow Diagram of Latent Heat Experimental Setup.

The heating input from the excitation of the TES must be approximately equal to and opposite to the heating output through the weak link. This is necessary to stabilize the beam at a certain temperature and reduce/remove temperature fluctuations. In the following calculations, it is assumed that the GE varnish and silver epoxy make negligible contributions, and that there is no temperature gradient across the silicon beam. The heating and cooling flows can be seen in Figure 6.3. The latent heat will be observed when the phase transition occurs. Saturation is taken into account as a potential problem which can be solved with computer controlled feedback. The fourth cause of heat flow is the possibility of eddy current heating once in the normal state.

1. Power from TES excitation:

   a) for a $100\mu A$ current applied to the quasi-voltage biased feedback circuit, and $R_{60\%} = 15\Omega$

   $$P = \frac{V^2}{R} = 2.6 * 10^{-11} Watts \tag{6.8}$$

   b) four wire measurement, 10μA excitation, and $R_{60\%} = 15\Omega$

   $$P = I^2 R = 15 * 10^{-10} Watts \tag{6.9}$$

2. Platinum-tungsten weak link.
   The value of the weak link is calculated by the length, cross-sectional area and material of the weak link, as well as the specific heat of the stage/sample. Using heat capacity values from Phillips and Keesoms work [31], [32]. Platinum-tungsten is typically used in our lab.

   a)

   $$\tau = \frac{C_{(silicon+zinc)}}{\kappa_{(Pt-W)}} \tag{6.10}$$

   Using $C_{(Si,0.743K)} = [(4.46 * 10^{-5} \frac{J}{molK}) \ /(28.09 \frac{g}{mol})] * 80mg$
   $= 126.96 * 10^{-9} \frac{J}{K}$

   and $C_{(Zn,0.743K)} = [(4.83 * 10^{-4} \frac{J}{mol*K})//(65.39 \frac{g}{mol})] * 22.4mg$
   $= 165.5 * 10^{-9} \frac{J}{K}$

   we determine that $C_\Sigma = C_{zinc} + C_{silicon} = 292.46 * 10^{-9} \frac{J}{K}$

$$\kappa_{(PtW,0.743K,0.7cm)} = \frac{l_0 T A}{\rho L} \tag{6.11}$$

Where ρ, the resistivity of platinum-tungsten wire was measured in our lab.
$= [(2.44 * 10^{-8} \frac{W\Omega}{K^2}) * (0.743K) * (\pi * 0.0025^2 cm^2)]/[(60\mu\Omega * cm) * (0.7cm)]$
$= 8.49 * 10^{-9} \frac{W}{K}$

$\tau = \frac{C_{(silicon+zinc)}}{\kappa_{(PtW)}} = 34.45$ seconds

b) The power from the weak link is :

$$\dot{Q} = \frac{A}{l} \int_{0.604K}^{0.743K} \kappa(T) dT \tag{6.12}$$

$\dot{Q} = 3.38 * 10^{-13} W$

3. Latent Heat of Zinc at 743 mK is :

$$L_{H(Zn,0.743K)} = \frac{B_{C0}^2 * V * [1 - (T/T_c)^2] * (T/T_c)^2}{2 * \pi * \mu_0} = 6.12 * 10^{-6} \frac{J}{mol} \tag{6.13}$$

where V is the atomic volume, B_0 is the critical magnetic field at zero Kelvin, μ_0 is permeability of free space ($4\pi * 10^{-7} \frac{Tm}{A}$) and T is the temperature and T_c (0.855 K) is the critical temperature at zero applied magnetic field.

Zinc values: B_0=53.4 Gauss, V=9.16$\frac{cm^3}{mol}$. The mass of our sample is 22.4 mg and the molar mass of zinc is 65.39$\frac{g}{mol}$ which gives us a expected $L_{H(Zn,0.743K)} = 1.35nJ$.

4. The expected temperature change in TES from L_H

$$\Delta T = \frac{E}{C} = \frac{L_H}{C_\Sigma} = 4.6\ mK \tag{6.14}$$

This temperature change is expected to be large, although this temperature change could be measured with conventional thermometers, as this is the first 'proof of principle' measurement, final measurements on heavy fermion samples are expected to be much smaller which will need the sensitivity of a TES.

Chapter 7

Latent Heat Results and Discussion

Many attempts were made to measure the latent heat of the superconducting transition and several setbacks were encountered along the way (broken leads, bad contacts, zinc sample detaching, etc.). In order to eliminate some potential problems, the setup was simplified by removing the feedback circuit. Even though previous measurements used the LTT feedback circuit (see Figure 4.6), its many components and contact points meant it had a higher chance of failure. Although this modified setup was not ideal, due to positive ETF and potential saturation in the normal region, it was found to be acceptable for detecting at least the signature of the latent heat of the superconducting transition of zinc. This was suitable for an initial attempt.

Latent heat data was obtained placing a zinc sample in the centre of a Helmholtz coil and ramping the magnetic field. The field was ramped from 0 G to 100 G, at rates from 0.1 G/sec to 0.4 G/sec. The current applied to the magnet did not to produce enough heating to make the magnet go normal and no distinct eddy current heating was observed.

7.1 Characterization of TES on silicon beam

The RuO_2 thermometer on the silicon beam had never been used before and needed to be calibrated. The calibration was found to be of the form $T = 10^{A*(logR)^3+B*(logR)^2-C*(logR)+D}$ where T is the temperature and R is the resistance of the RuO_2 thermometer.

The characterization of the TES on the silicon beam was done by applying heat to the stage and recording the temperature of the RuO_2 thermometer (see details in Section 5.1). The voltage read out across the TES, was recorded and was converted to resistance since the excitation current was known. The heater power was reduced at each temperature step until the whole transition was recorded (see Figure 7.1).

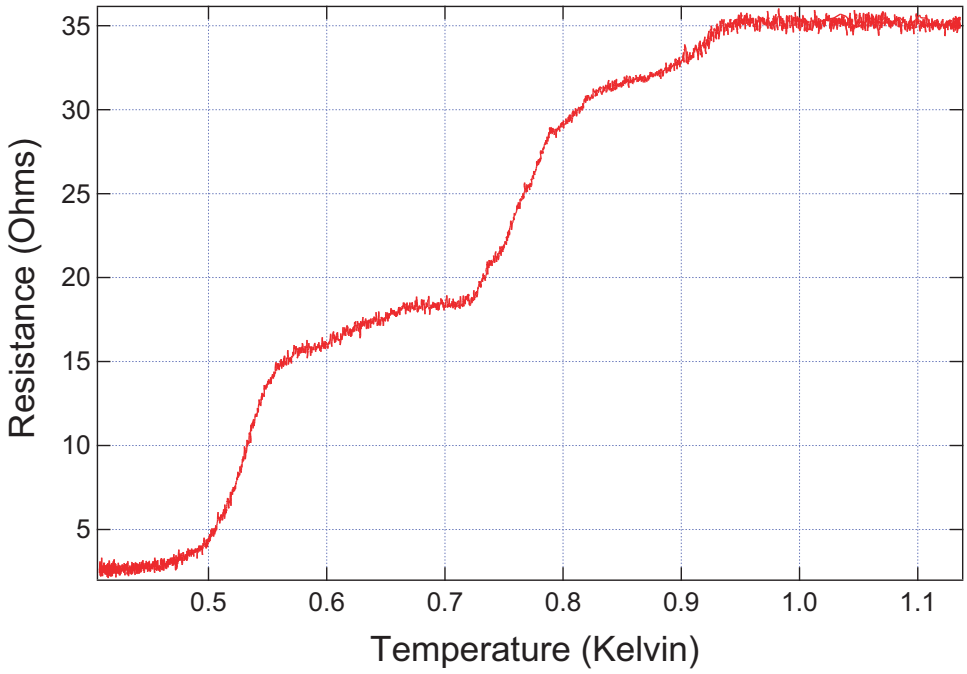

Figure 7.1: Temperature-resistance characterization of TES on silicon beam.

From Figure 7.1 it can be seen that the TES does not reach zero resistance, but a few Ohms, this has been found to be an additional resistance from the silver epoxy contacts on the TES. The transition curve looks abnormal compared to all other curves. There is some 'wobbliness' which was only observed in the two devices that were connected with silver epoxy instead of the aluminium wire-bonds previously used. It is unknown if this contributed to the abnormality or if it is just a coincidence. It was essential to fit a curve to this transition in order to have a function that could be used for converting resistance to temperature. A 20 term polynomial equation was found for a portion of the transition, which was used for the analysis in this Chapter. The residual resistance was found to be a maximum of 1.7 mK between the actual data and the best fit equation.

7.2 Thermal Conductance of Platinum-Tungsten Weak Link

Using the calibration found in Section 7.1 for the RuO_2 thermometer, the thermal conductance, K, was experimentally determined for the platinum-tungsten thermal weak link. This was done by using low voltage excitations on both the GRT thermometer attached to the stage and the RuO_2 thermometer attached to the silicon beam. Low voltage excitations reduce any self heating that may occur, which would give false temperature readings. The power moving through the platinum-tungsten wire is proportional to the product of its thermal conductivity and the temperature difference across it (between the silicon beam and the stage). Excitation power was applied to the TES and once thermal equilibrium was established the temperature difference was known for a given power. Various powers were applied to the TES and the resulting temperature changes observed. Figure 7.2 shows temperature difference as a function of power and the inverse slope is the thermal conductance.

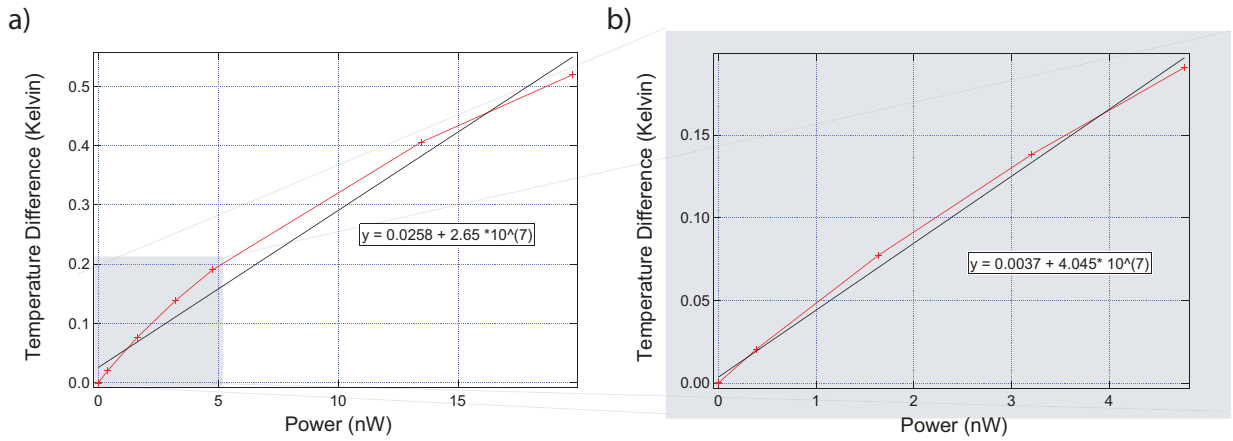

Figure 7.2: Determining the thermal conductance of the platinum-tungsten weak link.

$$\dot{Q} \; \alpha \; K\Delta T \tag{7.1}$$

$$K \; \alpha \; \frac{\dot{Q}}{\Delta T} \tag{7.2}$$

$$K = 37.88 * 10^{-9} \frac{W}{K} \tag{7.3}$$

From the Wiedemann-Franz law, the thermal conductivity is equal to the product of a constant and the temperature. The constant is proportional to the electrical conductance, which has both electron and phonon contributions. From the data shown in Figure 7.2a, this 'constant' was calculated and found in fact not to be a constant, but a function of temperature also. Using only the data in the temperature range used in the following experiments (Figure 7.2b) one finds a thermal conductance value closer to the theoretical expected value of 8.5 nW/K calculated in Section 6.5. The linear fit shown in Figure 7.2 shows an constant term as well as the slope. There should be no constant term. This shows that this measurement is not as accurate as it should be, there could be a correction needed to account for blackbody radiation contributions. The value of $K = 24.72 * 10^{-9} \frac{W}{K}$, found from the zoomed in data from Figure 7.2b will be used for the analysis in this Thesis.

7.3 Latent Heat Signature

Using the Lakeshore 370 temperature controller, the GRT thermometer on the ^{3}He Fridge stage was thermally stabilized such that the TES was biased at an optimum point on its transition. This was done with the temperature controller using PID feedback between the stage heater and the GRT thermometer. Although the TES voltage was typically recorded with an SRS 830 Lockin Amplifier via GPIB, in this case the signal from the lock-in amplifier was recorded with a data acquisition (DAQ) card which allowed faster sampling. This ensured that quick latent heat reactions were recorded to a high resolution. A function generator was used to ramp the field from 0 to 100 Gauss. This was done by sending the voltage output through a high wattage resistor to create the current which was proportional to the field in Gauss. The magnetic field ramping was done at various rates to explore the possibility of eddy current heating. Similar experiments done by Keesom and Van Laer [3] found eddy current heating to be a problem. It was reduced in these experiments by ramping the magnetic field slowly. The fact that we have not found eddy current heating to be a problem in our experiment may be due to sample size and shape. A needle shaped sample has potential for less eddy current heating than a sphere. Also, a sample with a higher mass has a larger surface area for a given geometry and thus more area for eddy currents to form.

7.3.1 Magnetic Field Sweep

The magnetic field was swept from 0 mA to 100 mA, corresponding to 0 to 100 Gauss, in anticipation of observing cooling and heating as the sample traversed from superconducting to normal and back to the superconducting state. Results are shown in Figure 7.3. The zinc starts in the superconducting state and the first downward/cooling peak corresponds to the phase change from superconducting to normal state at the critical magnetic field. The upward/heating peak occurs when the zinc returns from the normal state back to superconducting state. Four sweep rates were used with very similar results.

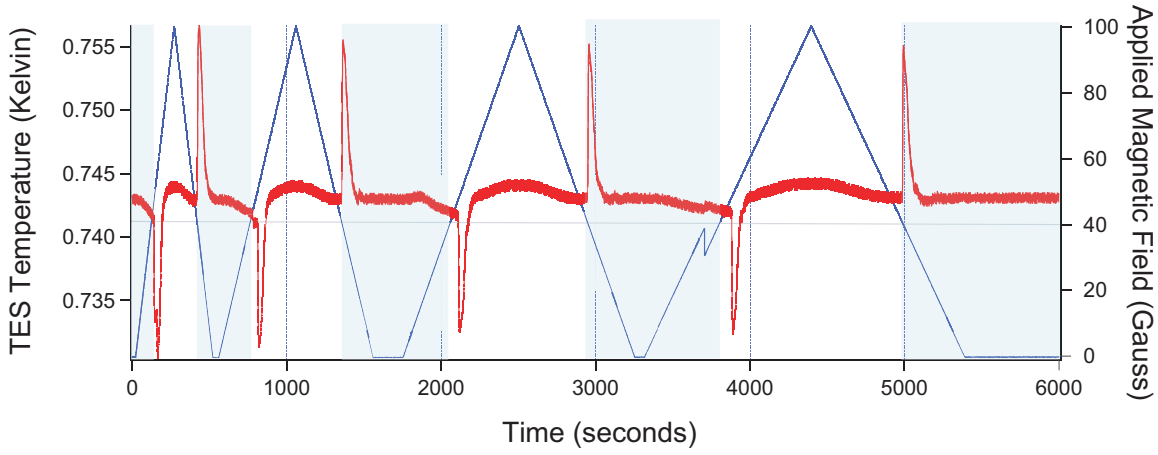

Figure 7.3: TES response to latent heat of superconducting transition as magnetic field is ramped. Sweep rates of 0.4 G/sec, 0.2 G/sec, 0.133 G/sec, 0.1 G/sec. Blue curve shows magnetic field ramping with time. Light blue background represents zinc in the superconducting state.

One interesting thing to notice from Figure 7.3 is that there is a rise observed in the TES response after the transition occurs. Initially thought that this would be due to eddy current heating. If it was eddy current heating, there would be a different heating observed for different magnetic field sweep rates. Comparing the TES output as a function of applied magnetic field can be seen in Figure 7.4. This shows that the 'heating' is the same for all sweep rates which eliminates eddy current heating as the cause. It could be due to a field dependence of the TES which will be explored further.

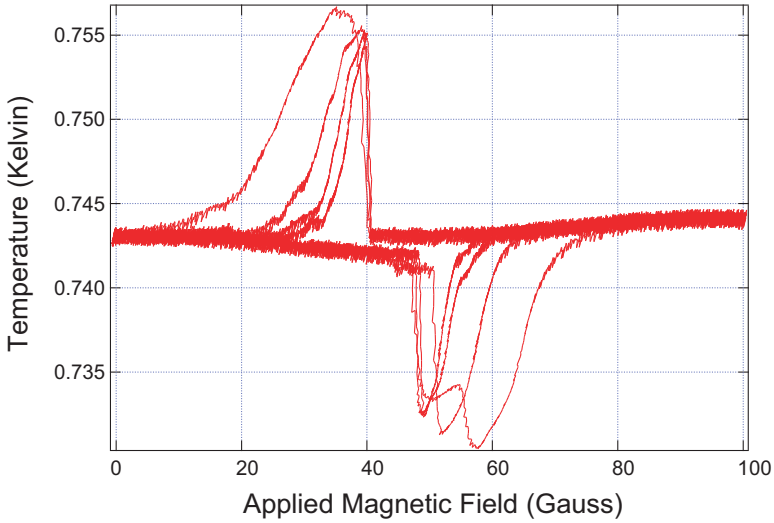

Figure 7.4: A closer look at the TES response to the latent heat of superconducting transition.

A second sweep from -100 mA to 100 mA was performed at a sweep rate of 0.2 G/sec to check for any offset or irregularities in the magnet and/or the function generator. Results from three cycles are shown in Figure 7.5. There is an additional cooling and heating pulse for each cycle as the critical field is passed two more times. Since positive critical field response is the same as negative critical field, no offset is necessary in further analysis.

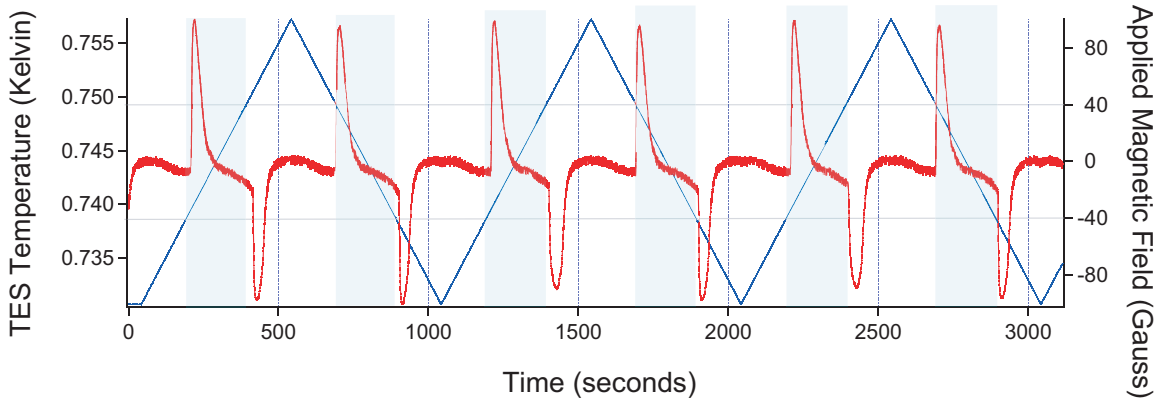

Figure 7.5: TES output as magnetic field is ramped positive and negative. Sweep rate was 0.2 G/sec. Blue curve shows magnetic field ramping with time. Light blue background represents the zinc in the superconducting state.

7.4 Noise

Looking closely at Figures 7.3 and 7.5, a resistance offset can be seen between the heating and cooling peaks depending on whether the zinc is in the superconducting or normal state. A first assumption is that in the normal state there is eddy current heating occurring which heats and stabilizes the TES to a higher resistance/temperature. However, after sweeping the field at various rates and observing the same offset each time, it is clear that this is not due to eddy current heating since it would vary with the rate of change of magnetic flux (increase with faster sweep rates). This offset was found to not be an heating equilibrium issue as waiting for a substantial time after the latent heat transition, the normal state does not approach the superconducting equilibrium.

7.4.1 TES Stability

Using the SRS 830 Lockin Amplifier in offset mode with 100x expansion, TES output was closely observed in the superconducting and normal states. This is shown in Figure 7.6. The magnetic field was swept four times, each at a different rate (0.4 G/sec, 0.2 G/sec, 0.133 G/sec and 0.1 G/sec) and the TES response was consistent. There is an interesting ripple as the zinc returns to the superconducting state, the cause of this is unknown at this time. There is a gradual latent heat slope before sharply reaching the peak, this may imply that not all of the zinc is going through the transition at the same time.

7.4.2 Normal State Sweep

To further understand what is causing the offset between the normal and superconducting states of zinc, the field was swept between 60 and 100 G. With this procedure the zinc remains in the normal state, but as seen in Figure 7.7 the TES is detecting heat in correlation with the field strength. As the field is reaching the maximum field the TES temperature is beginning to decrease, this is most likely due to temperature controller reacting to the change. Since the zinc is in the normal state, further work is needed to determine what else might be field dependent (perhaps the TES and/or GRT thermometer).

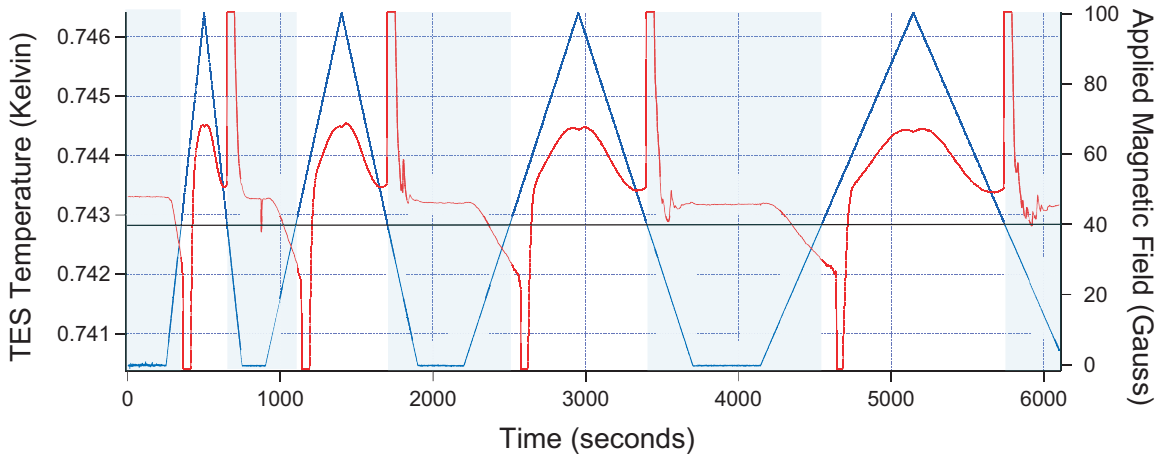

Figure 7.6: Expanded view of TES response to latent heat of superconducting transition. Sweep rates of 0.4G/sec, 0.2 G/sec, 0.133 G/sec and 0.1 G/sec were used. Blue curve shows magnetic field ramping with time. Light blue background represents zinc in the superconducting state.

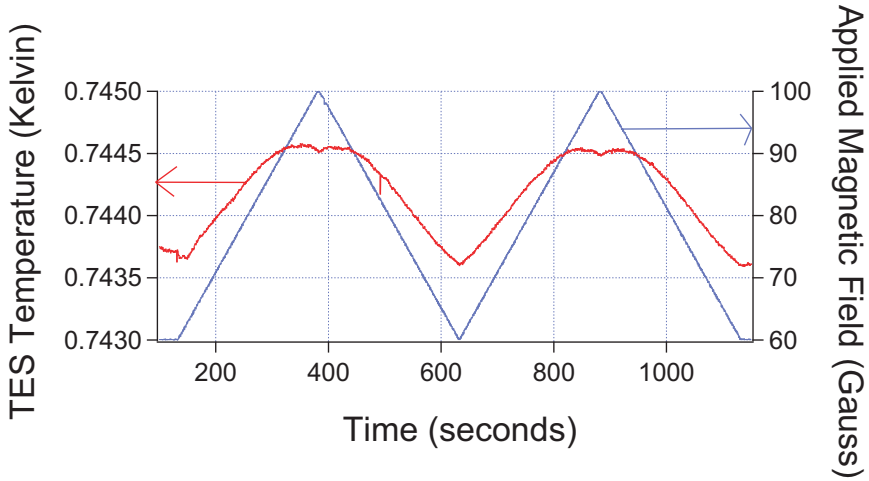

Figure 7.7: Magnetic field dependence of TES.

7.4.3 Field dependence with improved Lead Shielding

The original lead shield can be seen in Figure 6.1b. The end closest to the magnet is a full piece of lead with a small hole for the silicon beam to go through. From the end visible in the Figure, the lead shield does not make a complete loop and minor improvements made to the shield consisted of an additional strip of lead to complete the loop at the 'TES' end of the silicon beam.

The TES was biased on the transition, and the magnetic field ramped from 0 - 200 G. Figure 7.8 shows the TES response and no field dependence was observed. There was no repetitive signal as seen in Figure 7.7. There is much larger thermal noise fluctuations observed in Figure 7.8 than in Figure 7.7. This is due to the temperature controller configuration. When the GRT is operated at a higher voltage excitation, although self heating may occur, temperature stability increases. There was another difference between the two scenarios, in addition to the shielding improvement, the zinc was inside the lead shield for the second run. This was due to a setback in which some of the silicon which the zinc was attached to broke off, so to keep mass and heat capacity as consistent as possible, the zinc was moved inside the lead shield to test the new shielding. The fact that the field was swept from 0 to 200 G and no latent heat spikes were observed means that there is significant shielding improvement and the zinc observed less than 40 inside the lead shield (which was required previously to go from the superconducting state to the normal state). Shielding designs will need to be considered for further experiments as this is not an ideal design as the shield is soldered in place after the assembly is put together.

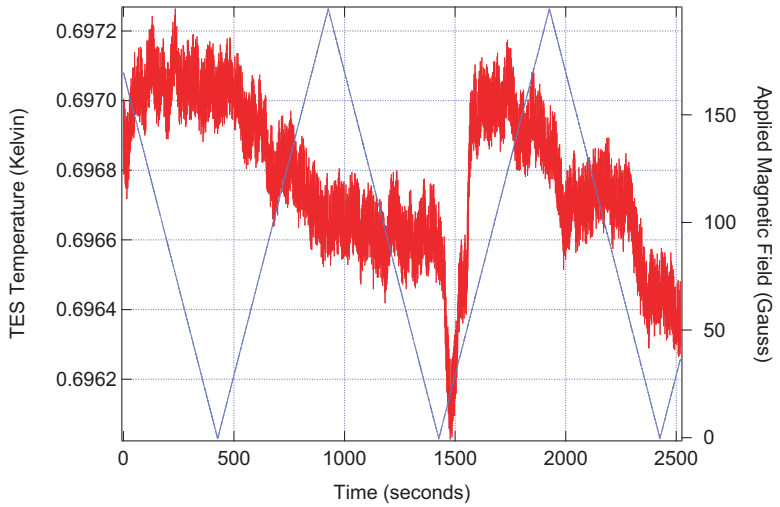

Figure 7.8: Magnetic field dependence of TES with improved lead shield.

7.4.4 Step

In an attempt to eliminate the additional heating/offset from the field dependent TES, the field was stepped instead of sweeping such that there was no gradual change in the field or zinc. It was expected that for smaller steps in field in close proximity to the critical field, there would be a smaller temperature/resistance offset. This was not found to be the case. The offset from Figure 7.9is 1.3 mK for a), 1.9 mK for b) and 1.5 mK for c).

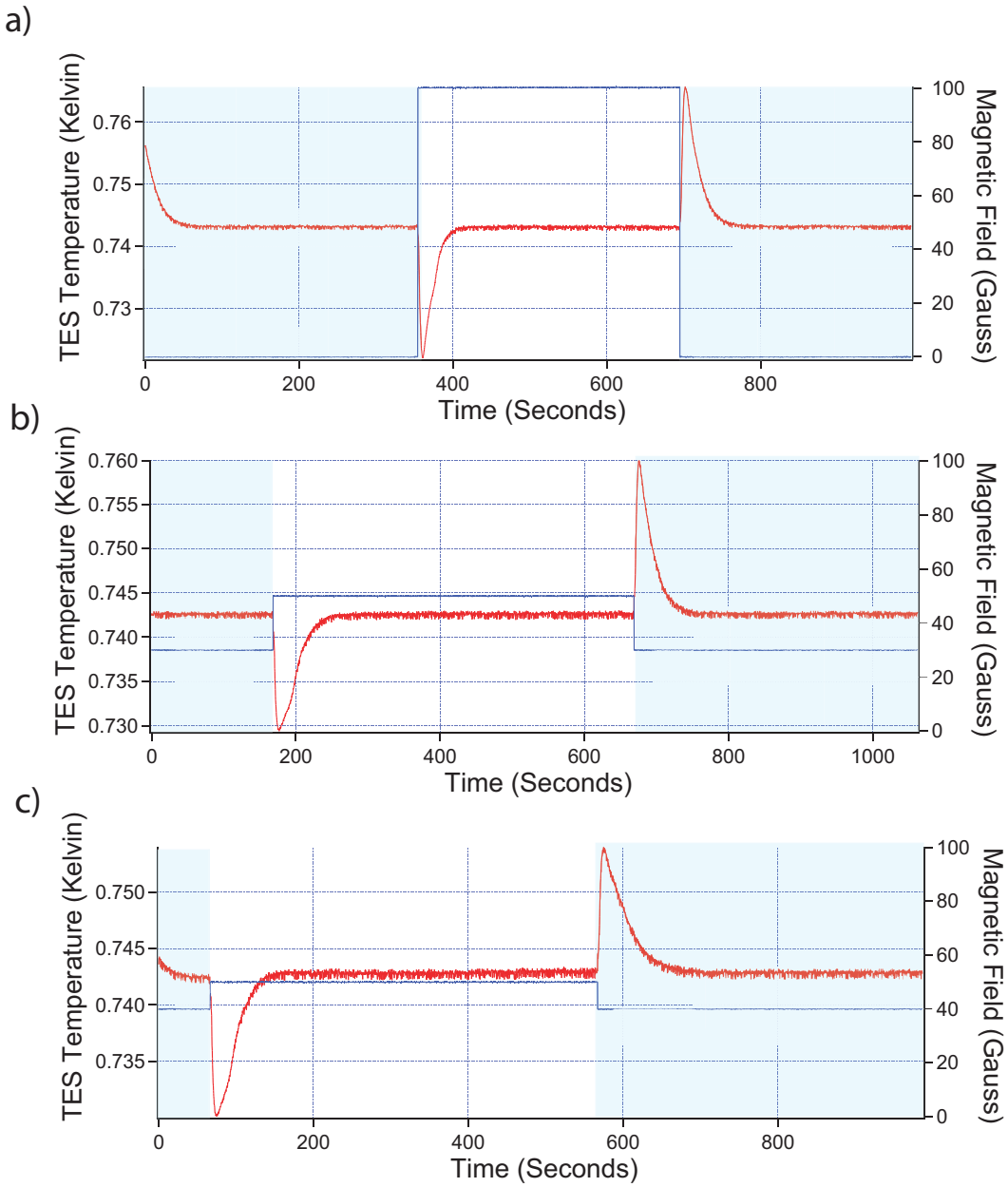

Figure 7.9: TES response from stepping magnetic field. a) step from 0 to 100 G, b) step from 30 to 50 G, c) step from 40 to 50 G. Blue curve shows magnetic field stepping with time. Light blue background represents zinc in the superconducting state.

7.5 TES Calibration

7.5.1 Due to Magnetic Field

The TES temperature function has been found to be a function of magnetic field also. This adds some additional error in the measurements shown in this Chapter. Comparing the sweep and step data it is easy to see that the latent heat is released in 'chunks' versus the one-shot step method. In order to account for the field dependence in the following analysis, the step data was analyzed instead of the sweep data which resulted in two distinct equilibrium states and they were assumed to be the same temperature.

Initially it was expected that the TES had a magnetic field dependence similar to that shown in Figure 7.10, that as a magnetic field is applied and then increased, the T_C will decrease. After using the data from Section 7.4.3 it is clear that more work needs to be done on this calibration, as the data does not conform to that assumption. In the following analysis, the magnetic field calibration will be applied as a percent change of the resistance, specifically for each data set.

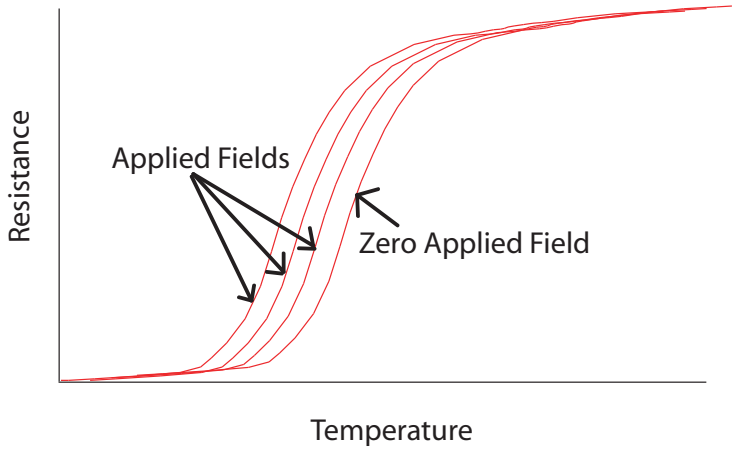

Figure 7.10: Expected TES output as a function of magnetic field.

7.5.2 Due to Power from TES Excitation

The power from the TES excitation must be taken into account the power as it is changing with resistance since we are current biased, we know the applied excitation and the power with its corresponding temperature difference is shown as a function of time in Figure 7.11 for the data in Figure 7.9c. This must be subtracted from the latent heat results before accurate analysis is complete. This is expected to make the heating and cooling peaks equal in magnitude to each other (as expected since this is a reversible transition).

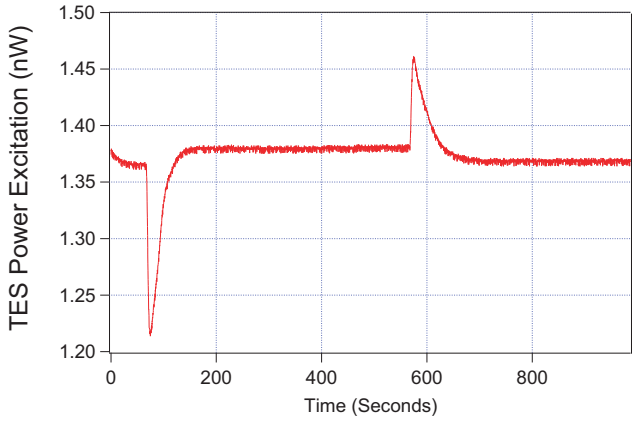

Figure 7.11: TES excitation power as a function of time for data shown in Figure 7.8c.

7.6 Determining the Power associated with the Latent Heat

The calibration from the magnetic field and the power from the TES excitation must be taken into account for determining the latent heat of superconducting transition of zinc. The total power is equal to the power supplied to the TES plus the power due to the latent heat. The total power is found from the temperature difference between the stage and the silicon multiplied by the thermal conductance which we have already found experimentally in Section 7.2. Figure 7.12 shows the power associated with the latent heat as a function of time for the same data as Figure 7.11 which is Figure 7.9c.

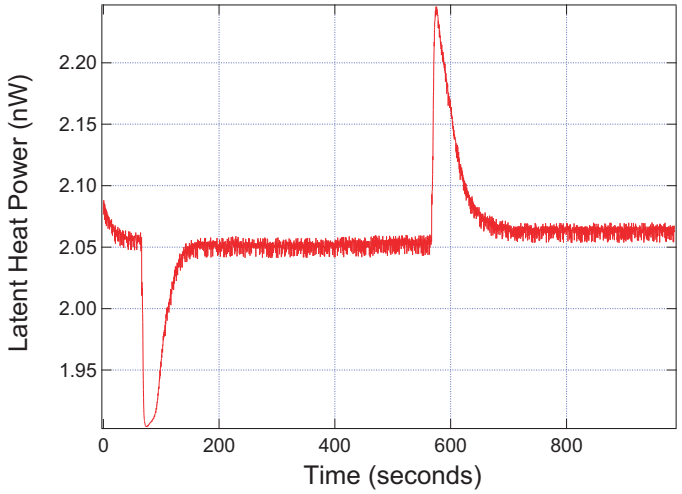

Figure 7.12: Latent heat power as a function of time for data shown in Figure 7.8c.

Since the y-intercept in Figure 7.12 is not zero, this indicates that there is a power contribution still not accounted for. This is most likely due to a blackbody radiation contribution. Assuming a one square centimeter opening in the lead shield, there is approximately 1.8 nW of power due to blackbody radiation assuming emissivity of 0.9 for silicon [33]. Accurate measurement of the silicon may account for the remaining error. There is a $Ru0_2$ thermometer mounted on the silicon beam but was not in use during these measurements and should not have a power contribution. The latent heat of transition for this sample of zinc can now be found by integrating the area under the curve. For the integration of the area under the curves which is the latent heat of the superconducting transition, the data is zero-ed and then integrated with Matlab. The average result for all data from Figure 7.9 was 6.0 nJ. This corresponds to 17.52 $\frac{\mu J}{mol}$.

7.7 τ, thermal weak link time constant

The latent heat of superconducting transition of zinc as a function of time is shown in figure 7.13. The exponential fit $y = Ae^{-t/\tau}$ is found where A is the temperature difference and τ is the relaxation time in seconds. Using the data from figure 7.3 and zooming in on the latent heat peak, an exponential fit is shown. Two curves are shown in Figure 7.13. These graphs have not taken the excitation power or the magnetic field dependence of the TES into account. The fit is not found to be a very good match and that is likely due to the fact that the field is swept. This may be due to sample shape or quality of sample.

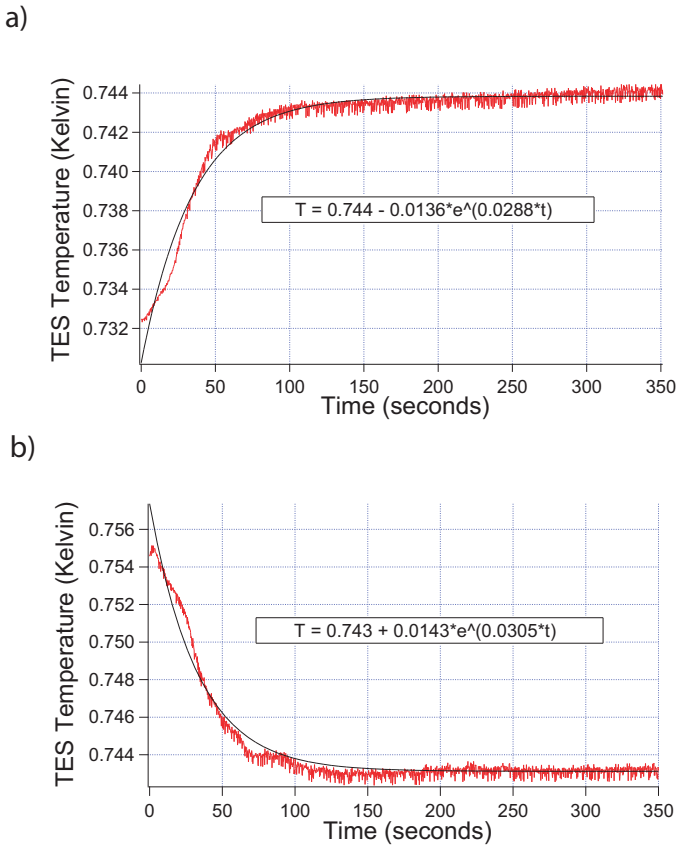

Figure 7.13: Exponential fits to peak s due to latent heat of transition. Equation for best fit is stated on each graph. a) Results of cooling transition from superconducting state to normal state. b) Heating due to latent heat of transition from normal to superconducting states.

The data in Figure 7.14, which is an analyzes version of the data from Figure 7.9c, has taken the magnetic field dependence of the TES into account. It can be seen that the double fit exponential are a better fit than those of the swept magnetic field shown in Figure 7.13. This is due to the fact that the magnetic field was stepped and the zinc went through the latent heat transition all at once. The fit is of the form $y = y_0 + A_1 e^{-t/\tau_1} + A_2 e^{-t/\tau_2}$, the first fit is that of the heat traveling through the silicon beam to the TES where it is detected, and the second fit is the latent heat transition data. Further calculations and final results presented in Section 7.7 and Section 7.8 use averaged data from Figure 7.9.

$$\tau = 17.0 \; seconds \tag{7.4}$$

$$\Delta T = 44.4 \; mK \tag{7.5}$$

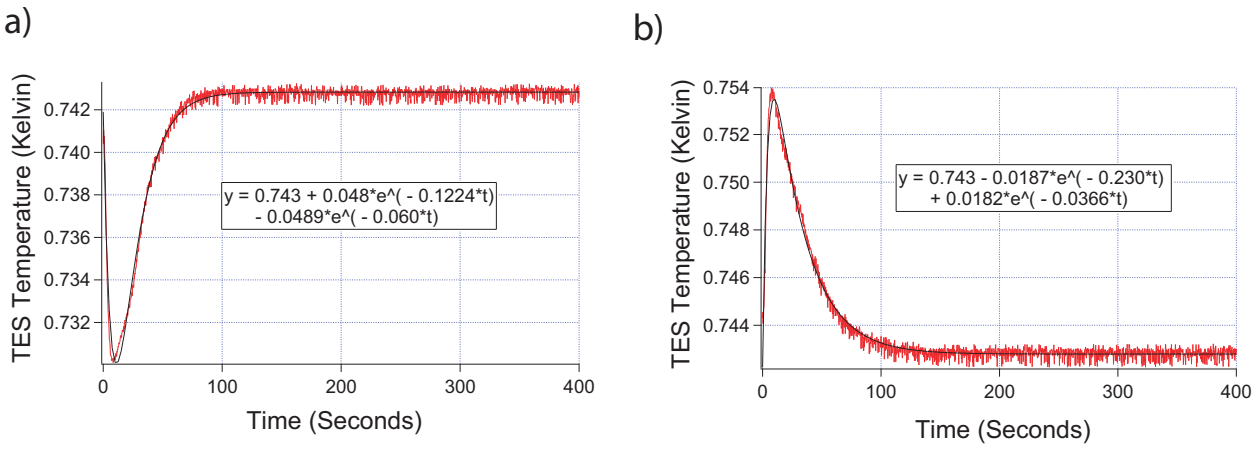

Figure 7.14: Double exponential fits to peaks from latent heat of transition. Equation for best fit is stated on each graph. a) Results of cooling transition stepped from superconducting to normal state. b) Heating due to latent heat of transition stepped from normal to superconducting states.

7.8 Experimental values of Latent Heat of superconducting zinc

Using K and τ found in Sections 7.2 and 7.6, C_Σ and L_H can now be determined.

$$C_\Sigma = \tau K = 420.24 * 10^{-9} \frac{J}{K} \tag{7.6}$$

$$L_H = C\Delta T = 18.65nJ = 54.47 * 10^{-6} \frac{J}{mol} \tag{7.7}$$

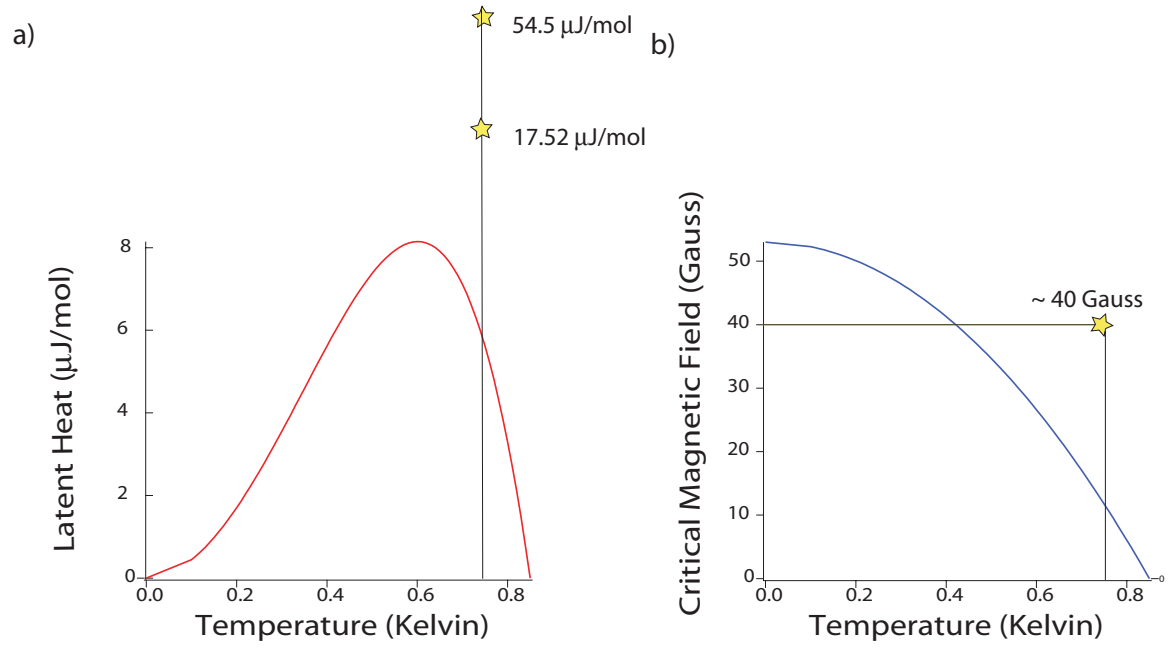

Figure 7.15: Zinc Results at 740 mK. a) Latent heat of superconducting transition. b) Critical magnetic field.

7.9 Comparison with expected theoretical results

The theoretical values found in Section 6.5 are shown in Table 7.1 as a comparison with the experimental values found in this Chapter. The experimental values are averaged from all the peaks in the data shown in Figure 7.9. There are two different methods used to determine the latent heat as were shown in Sections 7.6 and 7.7-8. The differences are found to be reasonable for a first attempt and will likely be improved in further experiments.

Table 7.1: Comparing theoretical and experimental values of Latent Heat Experiment

	Theoretical Values	Experimental Values	
		Section 7.6	Section 7.7 - 7.8
τ	34.45 seconds		17.0 seconds
C_Σ	$292.46 * 10^{-9} \frac{J}{K}$		$420.24 * 10^{-9} \frac{J}{K}$
K	$8.49 * 10^{-9} \frac{W}{K}$	$24.72 * 10^{-9} \frac{W}{K}$	$24.72 * 10^{-9} \frac{W}{K}$
ΔT	4.6 mK		44.4 mK
L_H	$6.12 * 10^{-6} \frac{J}{mol}$	$17.52 * 10^{-6} \frac{J}{mol}$	$54.47 * 10^{-6} \frac{J}{mol}$
$B_C(0.743K)$	13.1 Gauss	40 Gauss	40 Gauss

7.9.1 Potential sources of error

Discrepancy between sets of data and between theoretical and experimental results are not known for certain at this time. In the C_Σ calculations in Section 6.5, the GE varnish, silver epoxy, aluminium and palladium are considered to be negligible contributions when doing the theoretical calculations for heat capacity. This may explain why the heat capacity and thermal conductivity are experimentally larger than expected.

If the zinc is not in the center of the coils, then the magnetic field will be not what was expected. Also no demagnetization factor was applied during analysis to account for the shape of the sample used.

Chapter 8

Discussion and Conclusion

8.1 Transition Edge Sensors

TES's were fabricated with a high yield rate, resulting in 13 working sensors shown in Chapter 5. Characterization was done for each of these using a four wire current biasing method to determine the resistance-temperature correlation, normal state resistance, transition width, critical temperature, and alpha value. Additional characterization was done to explore the quasi-voltage biasing readout method. This readout method is anticipated to be used in latent heat measurements and will need further computer development. Further fabrication work on TES's is anticipated to produce a higher yield as many fabrication procedures are more understood, such as sputtering parameters.

8.2 Latent Heat

An experiment for measuring the latent heat of superconducting transitions was set up and preliminary results are presented in Chapter 7. The data acquired generally illustrated what was expected. As the magnetic field through the zinc sample was raised above the critical field, the zinc underwent a first order phase transition from the superconducting state to the normal state with an associated negative latent heat observed with the TES. There was additional and unexpected magnetic field dependance observed in the TES. This warrants further investigation and could possibly be improved by shielding. Initially there was a partial lead shield surrounding the TES which was slightly modified to include a full lead ring at each end of the cylindrical shaped shield. This resulted in no observable field dependence in the TES readout. The GRT is even further from the magnet than the TES and is also known to be field dependent. More work is needed to determine if the shielding for both thermometers or only the TES should be improved. Eddy current heating was expected to be a large concern for this experiment but none was observed to the best of our knowledge. It is now understood that stepping the field is better than sweeping the field and it is expected that for small steps in field it may be possible to achieve less or no temperature offset between superconducting and normal equilibrium states. Once the shielding issues are dealt with, this is expected to not be a concern.

For future and final latent heat measurements, a sharper TES with a small transition width should be fabricated and controlled by LTT quasi-voltage biased negative feedback. This would also include creating and testing computer controlled feedback software.

There are many factors which need to be addressed and many steps can be done together. The lead shielding must be addressed completely. Some work was done to see how a minor improvement changed the field dependence of the TES. A new shield design will need to be developed for significant improvement. The addition of a radiation shield will eliminate any heating contribution due to blackbody radiation. The mass of the zinc sample should be reduced to test the sensitivity of the system as future uses are expected to involve measurements of smaller energies. By changing the mass and comparing the results to those in this thesis, the ratio of masses consistency can be checked. The ratio of masses should equal the ratio of the latent heats. Before using the LTT in the quasi-voltage biased readout system, it may be useful to first use it as a amplifier. This would produce an increased signal with less noise than a room-temperature transformer. During the latent heat experiments shown in this thesis, only the TES and magnetic field were recorded to facilitate for fast data collection. It would be useful to record the temperatures from the GRT and RuO_2 thermometers to see if they are changing as the zinc is adsorbing/expelling heat into the system. This would be a relatively easy change to implement.

The sensitive measurement of latent heat in a superconducting transition is an attainable result based on the knowledge gained in this experiment, with many interesting results to follow.

Appendix A

Silicon Wafer Specifications

Silicon wafers were purchased from Virginia Semiconductor Inc.

Specifications, Item 1, (reference PO 77328)
Diameter: $50.8mm0.3mm$
Orientation: $< 100 > 0.9$
Dopant: Undoped
Resistivity: $> 20ohm - cm$
Cz
Primary Flat Length: $15.881.65mm$
Primary Flat Orientation: $< 110 > 0.9$
Secondary Flat Length: $8.01.65mm$
Secondary Flat Orientation: $180cw5$
Bow: $< 40m$
Center Thickness: $200m25m$ ULTRATHIN
Total Thickness Variation (5 point measurement): $< 10m$
Surface: Single side polished, backside etched
Micro Roughness: $< 18A$
Edge Round: None
Thermal Oxidation Layer (Wet Process): None
Additional Thin Film Specifications: None

Laser Marking: None
Additional Cutting or Machining: None
COC Required: Yes
Measurement Data Required: None
Other Specifications: None

Appendix B

^{3}He Fridge Cooldown Procedure

1. The samples are mounted and the continuity of wires must be checked. The wires must be secure in place to ensure that there is no possibility of any contact with the vacuum can.

2. The vacuum can is placed over stage and guts of the fridge, sealing with a hand-made indium o-ring. The vacuum can is tightened in a star position to ensure even pressure on all sides of the indium.

3.
   - The vacuum can is pumped out and then filled with a few Torr of neon gas which is used as exchange gas to help cool the interior of the fridge.
   - The 1K pot is also pumped out and then flushed with helium gas, pumped out again and then left over pressured with helium gas. This ensures that there is no moisture in the 1K pot which would freeze once the system is cooled.
   - The dewar jacket must also be pumped out prior to use (or every few cool downs) and when suspected of lacking a good vacuum.

4. The nitrogen jacket and dewar interiors are pre-cooled with liquid nitrogen, usually overnight but 4-6 hours is sufficient.

5. The cryostat is lowered into the nitrogen filled dewar ensuring that there is contact between the sleeve and 77K baffles and left to cool overnight with the dewar. It is

more efficient (in terms of amount of nitrogen required) to have the cryostat sit above the nitrogen and be vapour cooled instead of immersed in the liquid.

6. The nitrogen in the main dewar compartment must be removed. Using a long thin walled stainless steel tube placed all the way to the bottom of the dewar and over pressuring the dewar with helium gas, all the nitrogen is forced out of the stainless steel tube.

7. Once all the nitrogen is removed, the charcoal flow line capillary must be flushed with helium gas to ensure that there is no water or liquid nitrogen in the capillary. This ensured that nothing is frozen during the following helium transfer. A similar action is done with the overpressured 1K pot. Opening the needle valve helium gas which is overpressuring the 1K pot will flow into the dewar. This cannot be done visually as in the case of the charcoal, but as long as the 1K pot has been overpressured, all moisture is removed from the capillary. This is important as any blockages which occur in these capillaries will end the cool down.

8. A slow liquid helium transfer is now done to further cool the fridge via the neon exchange gas which is inside the vacuum can. It is possible to cool to approximately 20 Kelvin, at which point the neon will freeze and the remainder of cooling is achieved only by weak thermal contact.

9. The helium transfer continues and fills the remainder of dewar with liquid helium.

10. Once the transfer is complete, the warm helium gas which is currently in the 1K pot must be pumped out and the needle valve opened to allow cold liquid helium into the 1K pot chamber. The pressure can be adjusted by opening or closing the needle valve. It is important to have the needle valve open enough that the 1K pot is cooling or cold, but not open too far that the pump has to work harder than necessary.

11. Once the 1K pot is cold, reaching 1.2 Kelvin, the ^{3}He can be condensed into the ^{3}He pot. The ^{3}He is contained in a closed system involving the ^{3}He pot, charcoal, and a reservoir. Since the system is currently cold, all the ^{3}He is adsorbed on the charcoal. Heating the charcoal to 40 Kelvin using 3.5V applied to the heater, the

^{3}He is released and since the 1K pot is cold, it cools the ^{3}He allowing it to drip down into the ^{3}He pot and accumulate. Once the ^{3}He has accumulated in the ^{3}He pot, its temperature will stabilize near 1.8 Kelvin, depending on the heat load. At this point the flow meter can be opened. This allows cold helium to flow in the capillary wound around the charcoal, cooling the charcoal and causing it to pump the ^{3}He. The ^{3}He pot can now cool to as low as 250 mK.

12. At the end of the experiment.

    - Raise cryostat out of dewar.
    - Place plastic around fridge to minimize condensation. This is especially important for quick turnaround time between cool downs.
    - Flush helium portion of dewar with liquid nitrogen to reduce/limit any helium gas diffusion through the fiberglass membrane into the jacket space.

Appendix C

TES Collection

This is a summary of working TES's in our lab, for reference use. Resistance-Temperature plots, current whereabouts, size, date made, issues encountered, any other useful information for the future.

- **Mr20A**

  This Device is mounted on a silicon beam and was planned to be used for the latent heat experiment. No further work was done.

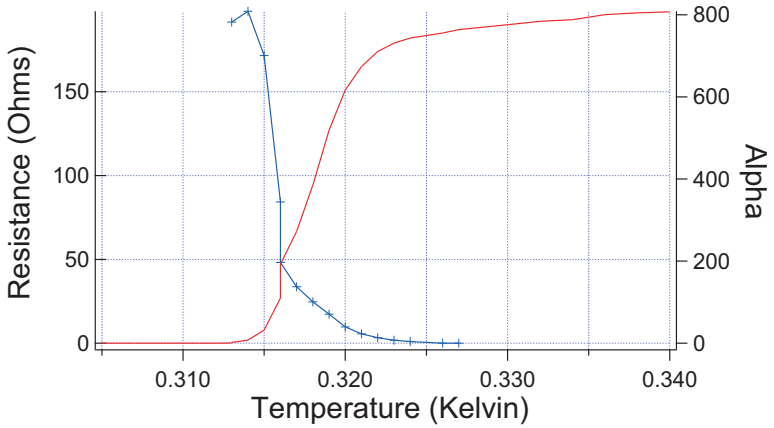

Figure C.1: TES ID:Mr20A Characteristics. Resistance and alpha versus temperature.

Table C.1: Mr20A Sputtering Information

Fabrication Date(s)	March 20, 2006
Flow Rate	74.1
Pressure	$1.3 * 10^{-2}$ mbar
Aluminium	700 V, 6 minutes, 130 mA, 19% 5 kV
Wait Time	1 minute
Palladium	700 V, 1.5 minutes, 130 mA, 17% 5 kV
Number of devices	1

- **Ap11J**

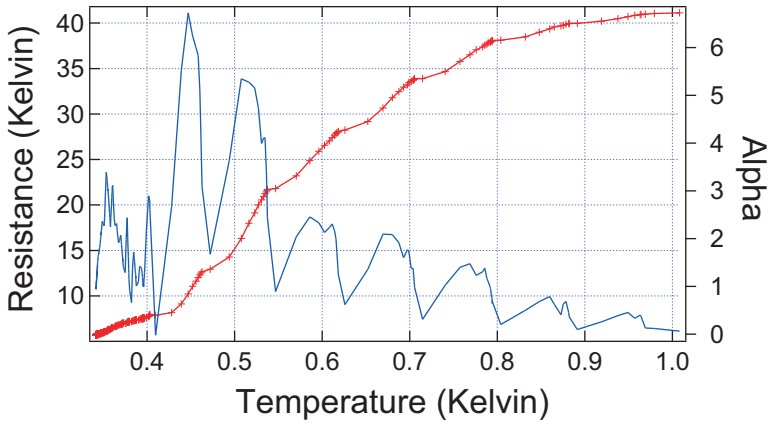

Figure C.2: TES ID:Ap11J Characteristics. Resistance and alpha versus temperature.

Table C.2: Ap11J Sputtering Information

Fabrication Date(s)	April 7-11, 2006
Flow Rate	74.1
Pressure	$1.4 * 10^{-2}$ mbar
Aluminium	700 V, 6 minutes,135 mA, 19% 5 kV
Wait Time	unknown
Palladium	700 V, 1.5 minutes, 125 mA, 18.2% 5 kV
Number of devices	1

- **Ap11L-a**

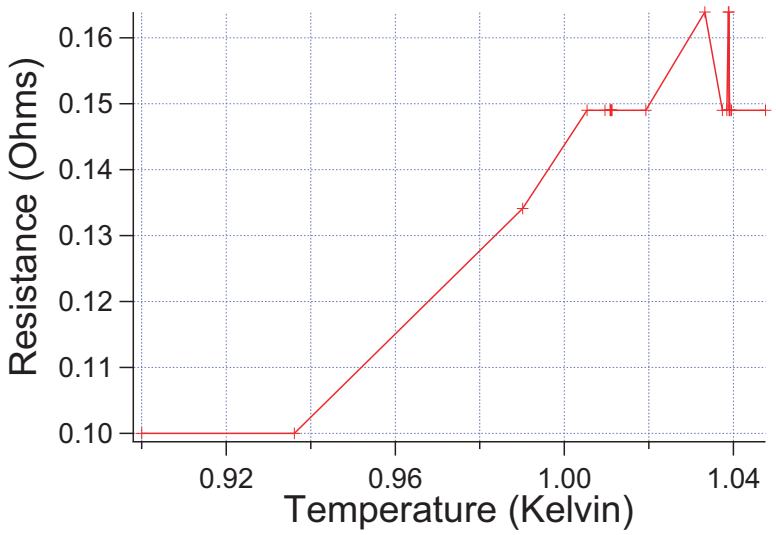

Figure C.3: TES ID:Ap11L-a Characteristics. Resistance versus temperature.

Table C.3: Ap11L-a Sputtering Information

Fabrication Date(s)	April 7-11, 2006
Flow Rate	unknown
Pressure	unknown
Aluminium	6 minutes
Wait Time	unknown
Palladium	1.5 minutes
Number of devices	1

- **Ap11L-b**

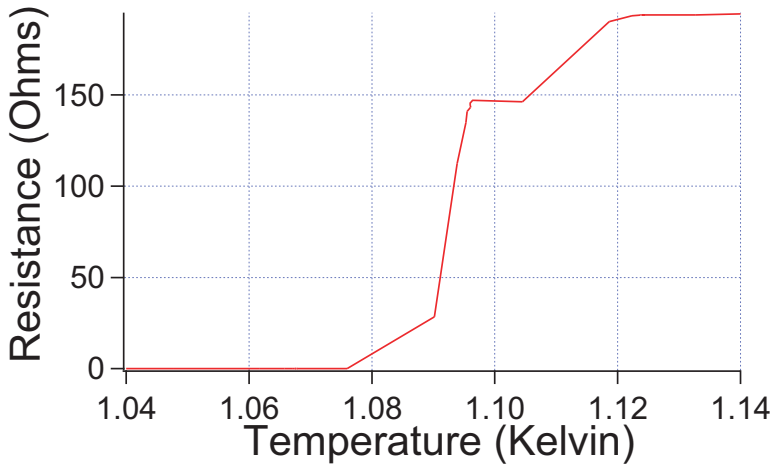

Figure C.4: TES ID:Ap11L-b Characteristics. Resistance versus temperature.

Table C.4: Ap11L-b Sputtering Information

Fabrication Date(s)	April 7-11, 2006
Flow Rate	unknown
Pressure	unknown
Aluminium	6 minutes
Wait Time	unknown
Palladium	1.5 minutes
Number of devices	1

- **JL15B**

  Mounted on silicon beam with Epo-tek H20E silver epoxy, baked, and transition was no longer attainable, upon further attemps to find the transition, the pads of the TES were joined with silver epoxy by accident. This TES is no longer useable for any purpose.

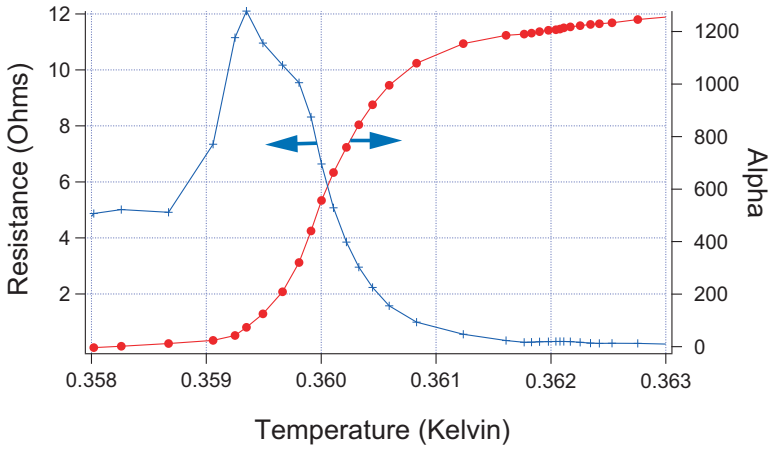

Figure C.5: TES ID:JL15B Characteristics. Resistance and alpha versus temperature.

Table C.5: JL15B Sputtering Information

Fabrication Date(s)	July 13-15 2006
Flow Rate	72.5
Pressure	$1.3 * 10^{-2}$ mbar
Aluminium	800 V, 2 minutes, 150 mA, 22% 5 kV
Wait Time	2 minutes
Palladium	800 V, 20 seconds, 150 mA, 20% 5 kV
Number of devices	1

- **Au02A**

  This device was planned to be connected with NbTi wires with EpoTek H20E Silver epoxy and baked to see if it was destroyed the same as JL15B was. I don't know if this was ever fully completed. Check status.

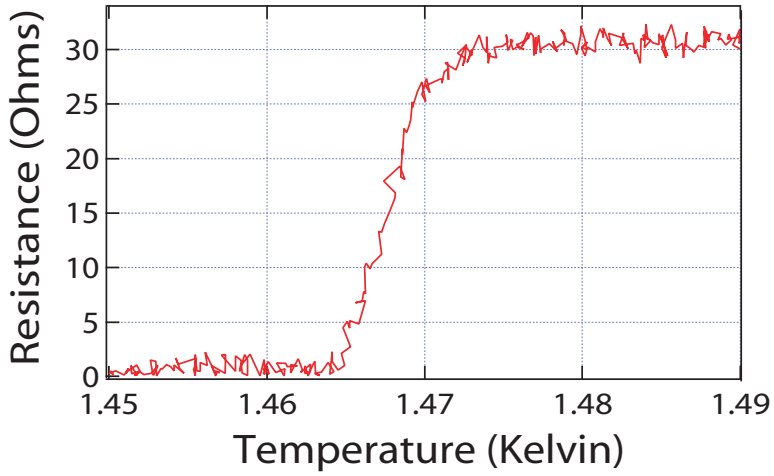

Figure C.6: TES ID:Au02A Characteristics. Resistance versus temperature.

Table C.6: Au02A Sputtering Information

Fabrication Date(s)	August 1-2, 2006
Flow Rate	74.1
Pressure	$1.4 * 1-^{-2}$ mbar
Aluminium	800 V, 2 minutes, 160 mA, 22% 5 kV
Wait Time	2 minutes
Palladium	800 V, 10 seconds, 150 mA, 20% 5 kV
Number of devices	1

- **AuO2B**

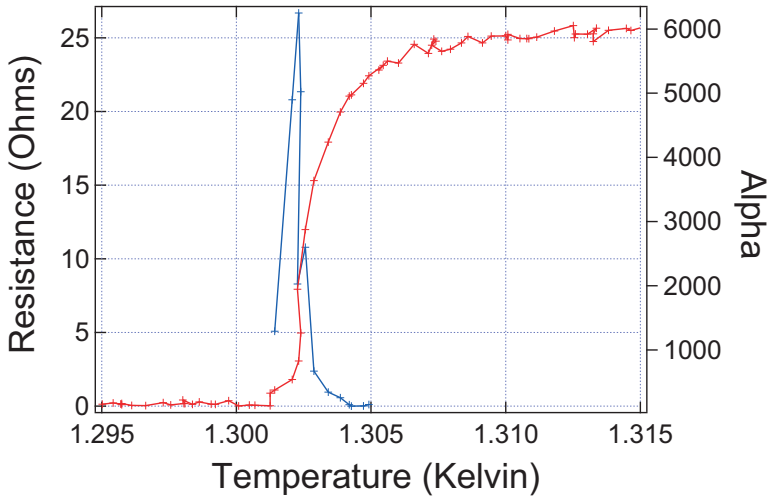

Figure C.7: TES ID:Au02B Characteristics. Resistance and alpha versus temperature.

Table C.7: Au02B Sputtering Information

Fabrication Date(s)	August 1-2, 2006
Flow Rate	74.1
Pressure	$1.4 * 10^{-2}$ mbar
Aluminium	800 V, 2 minutes, 160 mA, 22% 5 kV
Wait Time	2 minutes
Palladium	800 V, 10 seconds, 150 mA, 20% 5 kV
Number of devices	1

- **Au04A**

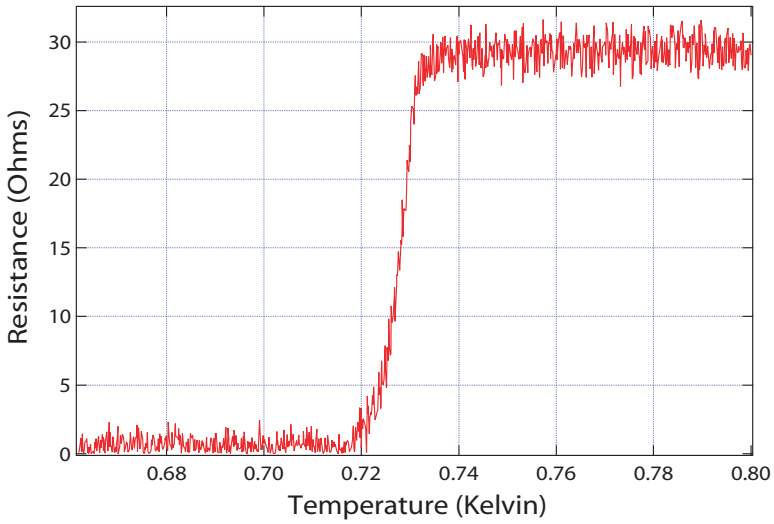

Figure C.8: TES ID:Au04A Characteristics. Resistance versus temperature.

Table C.8: Au04A Sputtering Information

Fabrication Date(s)	August 1-4, 2006
Flow Rate	74.1
Pressure	$1.4 * 10^{-2}$ mbar
Aluminium	800 V, 2 minutes, 160 mA, 22% 5 kV
Wait Time	2 minutes
Palladium	800 V, 20 seconds, 150 mA, 20% 5 kV
Number of devices	1

- **Au04B**

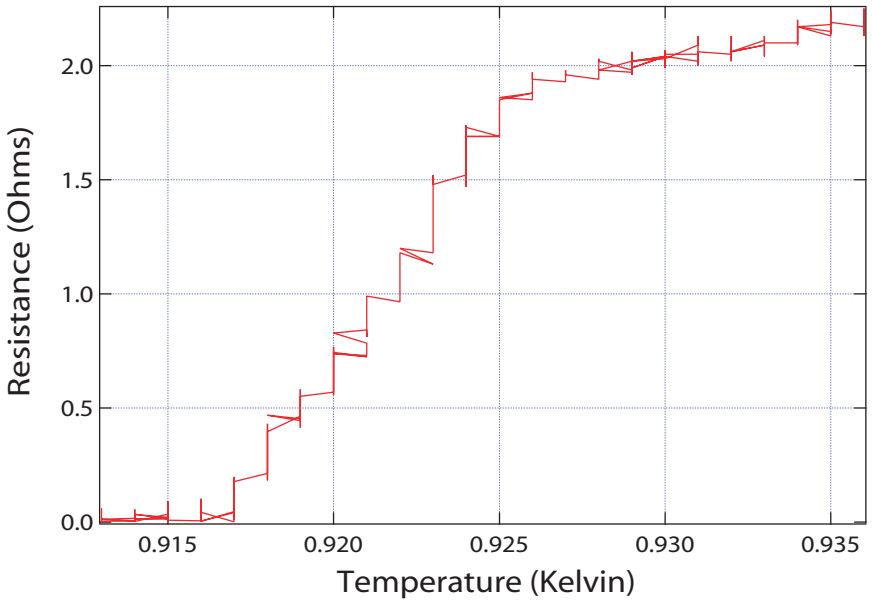

Figure C.9: TES ID:Au04B Characteristics. Resistance versus temperature.

Table C.9: Au04B Sputtering Information

Fabrication Date(s)	August 1-4, 2006
Flow Rate	74.1
Pressure	$1.4 * 10^{-2}$ mbar
Aluminium	800 V, 2 minutes, 160 mA, 22% 5 kV
Wait Time	2 minutes
Palladium	800 V, 15 seconds, 150 mA, 20 % 5 kV
Number of devices	1

- **D12A5**

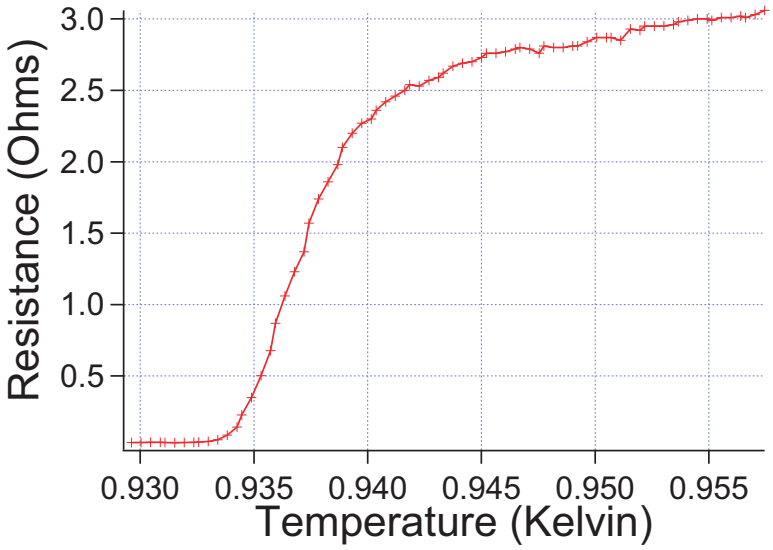

Figure C.10: TES ID:D12A5 Characteristics. Resistance versus temperature.

Table C.10: D12A3 Sputtering Information

Fabrication Date(s)	December 12, 2006
Flow Rate	74.1
Pressure	$1.4 * 10^{-2}$ mbar
Aluminium	800 V, 2 minutes, 150 mA, 22% 5 kV
Wait Time	4 minutes
Palladium	800 V, 10 seconds, 150 mA, 20% 5 kV
Number of devices	5

- **N29C**

Table C.11: N29C Sputtering Information

Fabrication Date(s)	November 29, 2007
Flow Rate	74.1
Pressure	$1.3 * 10^{-2}$ mbar
Aluminium	800 V, 2 minutes, 160 mA, 22% 5 kV
Wait Time	2 minutes
Palladium	800 V, 20 seconds, 160 mA, 20% 5 kV
Number of devices	30

N29C-a Excellent

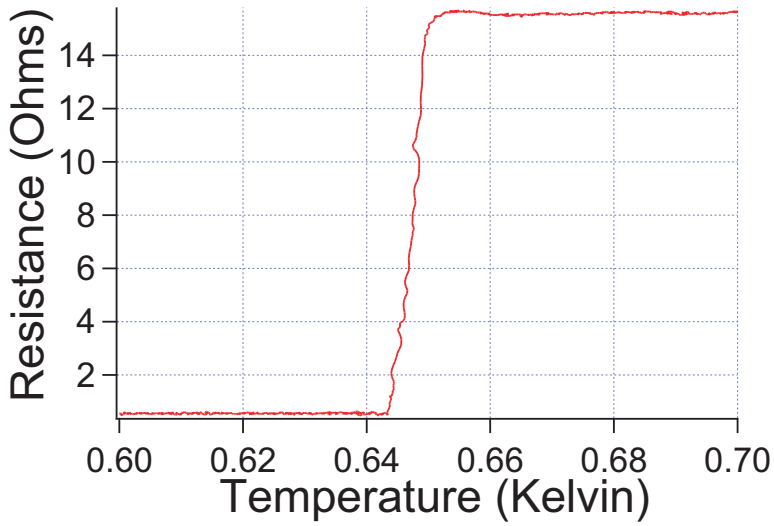

Figure C.11: TES ID:N29C-a Characteristics. Resistance versus temperature.

N29C-b GE varnished to silicon beam, silver epoxy 4110 and NbTi filaments were used to make electrical connections. Currently used in latent heat experimental setup. There is a 'wobbliness' in this transition curve.

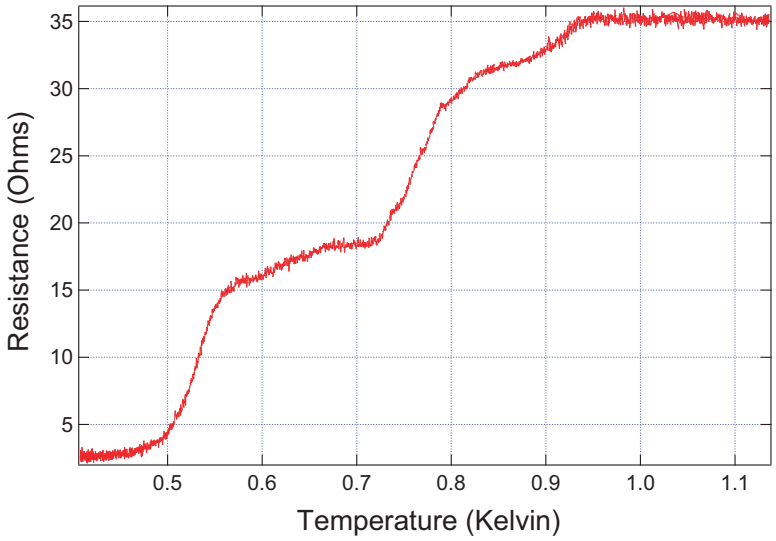

Figure C.12: TES ID:N29C-b Characteristics. Resistance versus temperature.

N29C-c Typical four wire measurements done with the difference that epotek 4110 silver epoxy was used for electrical connections. This was done to ensure that this was not a potential problem of why the latent heat setup was not working. There is a 'wobbliness' in this transition curve, similar to that seen in N29C-b.

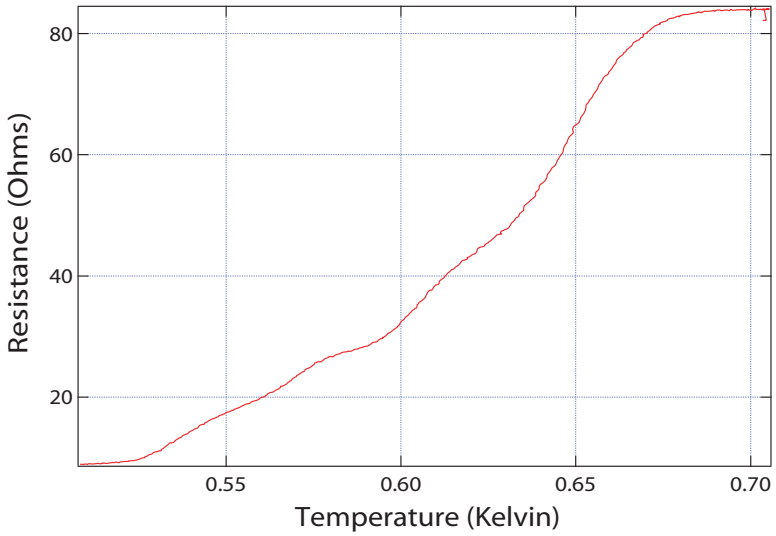

Figure C.13: TES ID:N29C-c Characteristics. Resistance versus temperature.

Bibliography

[1] Francis A. Shunk, editor. *Constitution of Binary Alloys, Second Supplement*. McGraw Hill, 1965.

[2] A.J. Walton, W. Parkes, J.G. Terry, C. Dunane, J.T.M. Stevenson, A.M. Gundlach, G.C. Hilton, K.D. Irwin, J.N. Ullom, W.S. Holland, W.D. Duncan, M.D. Audley, P.A.R Ade, R.V. Sudiwala, and E. Schulte. Design and fabrication of the detector technology for SCUBA-2. *IEE Proc.-Sci. Meas. Technol.*, 151, 2004.

[3] W. H. Keesom and P. H. Van Laer. Measurements of the latent heat of tin while passing from the superconductive to the non-superconductive state at constant temperature. *Physica*, IV:487–493, 1937.

[4] R. D. Parks, editor. *Superconductivity*. Marcel Dekker, Inc. New York, 1969.

[5] W.S. Holland, E.I. Robson, W.K. Gear, C.R. Cunningham, J.F. Lightfoot, T. Jennes, R.J. Ivison, J.A. Stevens, P.A.R. Ade, M.J. Griffin, W.D. Duncan, J.A. Murphy, and D.A. Naylor. SCUBA: A common-user submillimetre camera operating on the James Clerk Maxwell Telescope. *Mon. Not. R. Astron. Soc*, 303:659–672, 1999.

[6] K.D.Irwin, S. W. Nam, B. Cabrera, and B Chung. A quasiparticle-trap-assisted transition-edge sensor for phonon-mediated particle detection. *Review of Scientific Instruments*, 66, 1995.

[7] S.H. Moseley, J.C. Mather, and D. McCammon. Thermal detectors as X-ray spectrometers. *Journal of Applied Physics*, 56:1257, 1984.

[8] D.A. Wollman, K.D.Irwin, G.C.Hilton, L.L Dulcie, D.E. Newbury, and J.M. Martinis. High-resolution, energy-dispersive microcalorimeter spectrometer for X-ray microanalysis. *Journal of Microscopy*, 188:196–223, 1997.

[9] K.D. Irwin, G.C.Hilton, John M. Martinis, S. Deiker, N. Bergren anad S. W. Nam, D. A. Rudman, and D. A. Wollman. A Mo-Cu superconducting transition-edge microcalorimeter with 4.5 eV energy resolution at 6 keV. *Nuclear Instruments and Methods in Physics Research, Section A*, 444:184–187, 2000.

[10] Norman E. Booth, Blas Cabrera, and Ettore Fiorini. Low-Temperature Particle Detectors. *Annual Review of Nuclear and Particle Science*, 46:471–532, 1996.

[11] U. Nagel, A. Nowak, H.-J. Gebauer, P.Colling, S.Cooper, D.Dummer, P.Ferger, M.Frank, J.Igalson, A.Nucciotti, F. Probst, W.Seidel, E.Kellner, F.v. Feilitzsch, and G.Forster. Proximity effect in iridium-gold bilayers. *Journal of Applied Physics*, 76:4262, 1994.

[12] G. W. Fraser. On the nature of the superconducting-to-normal transition in transition edge sensors. *Nuclear Instruments and Methods in Physics Research, Section A*, 523:234–245, 2004.

[13] J. N. Ullom, J.A.Beall, W. B. Doriese, W.D.Duncan, L. Ferreira, G.C. Hilton, K.D.Irwin, C.D.Reintsema, and L.R.Vale. Optimizated transition-edge X-ray microcalorimetry with 2.4 eV energy resolution at 5.9 keV. *Applied Physics Letters*, 87:194103, 2005.

[14] D.A. Wollman, S.W.Nam, D.E.Newbury, G.C. Hilton, K.D. Irwin, N.F. Bergren, S. Deiker, D.A. Rudman, and J.M. Martinis. Superconducting transition-edge-microcalorimeter X-ray spectrometer with 2 eV energy resolution at 1.5 keV. *Nuclear Instruments & Methods in Physics Research, Section A*, 444:145–150, 2000.

[15] T.C. Chen, F.M. Finkbeiner, A. Bier, and B. DiCamillo. Molybdenum-gold proximity bilayers as tranition edge sensors for microcalorimeters and bolometers. *Superconductor Science and Technology*, 12:840–842, 1999.

[16] http://hyperphysics.phy astr.gsu.edu/Hbase/solids/chrlen.html. Internet Source, 2008.

[17] John Martinis, G.C.Hilton, K.D.Irwin, and D.A.Wollman. Calculation of Tc in a normal-superconductor bilayer using the microscope-based Usadel theory. *Nuclear Instruments and Methods in Physics Research, Section A*, 444:23–27, 2000.

[18] A.T. Lee, B. Cabrera, B.L.Dougherty, M.J. Penn, and J.G.Pronko. Measurements of the Ballistic Phonon Component Resulting from Nuclear Recoils in Crystalline Silicon. *Physical Review Letters*, 71:1395–1398, 1993.

[19] W.S. Holland, W.D. Duncan, B.D. Kelly, K.D. Irwin, A.J. Walton, P.A.R. Ade, and E.I. Robson. SCUBA-2: A large format submillimetre camera on the James Clerk Maxwell Telescope. *Proceedings of SPIE*, 4855:1–18, 2003.

[20] Siegfried Ewert. A demonstration experiment on the phase transition of a superconductor in a magnetic field. *European Journal of Physics*, 8:161–163, 1987.

[21] Frank Pobell. *Matter and Methods at Low Temperatures*. Springer-Verlag, 1992.

[22] Patrick de Perio. Developing a Low Noise, High Speed and Sensitivity Electronic Readout for Low Temperature Applications. Technical report, University of Waterloo, 2008.

[23] Jeffrey A. Quilliam. Specific Heat of the Dilute, Dipolar-Coupled, Ising Magnet LiHo(x)Y(1-x)F(4). Master's thesis, University of Waterloo, 2006.

[24] R. Movshovich, M. Jaime, J.D. Thompson, C. Petrovic, Z. Fisk, P.G. Pagliuso, and J.L. Sarrao. Unconventional Superconductivity in CeIrIn5 and CeCoIn5: Specific Heat and Thermal Conductivity Studies. *Physical Review Letters*, 86:5152–5155, 2001.

[25] P. G. Pagliuso, R. Movshovich, A. D. Bianchi, M. Nicklas, N. O. Moreno, J. D. Thompson, M. F.Hundley, J.L. Sarrao, and Z. Fisk. Multiple phase transitions in Ce(Rh,Ir,Co)In5. *Physica B*, 312-313:129–131, 2002.

[26] F. Ronning, C. Capan, E.D. Bauer, J.D. Thompson, J.L. Sarrao, and R. Movshovich‘. Pressure study of quantum critically in CeCoIn5. *Physical Review B*, 73, 2006.

[27] R. A. Fisher, S. Kim, B. F. Woodfield, N. E. Phillips, L. Taillefer, K. Haselbach, J. Flouquet, A.L. Giorgi, and J. L. Smith. Specific heat of UPt3: Evidence for Unconventional Superconductivity. *Physical Review Letters*, 62:1411–1414, 1989.

[28] Matthais J. Graf and Daryl W. Hess. Antiferromagnetic Domains and Superconductivity in UPt3. *Physical Review B*, 63:134502, 2001.

[29] H.H. Sample and L.G. Rubin. Instrumentation and methods for low temperature measurements in high magnetic fields. *Cryogenics*, pages 597–606, 1977.

[30] L.J. Neuringer, A.J. Perlman, L.G. Rubin, and Y. Shapira. Low Temperature Thermometry in High Magnetic Fields. II Germanium and Platinum Resistors. *The Review of Scientific Instruments*, 42, 1971.

[31] Norman E. Phillips. Heat Capacity of Superconducting Zinc. *Physical Review Letters*, 1:363–365, 1958.

[32] P.H. Keesom and G. Seidel. Specific Heat of Germanium and Silicon at Low Temperatures. *Physics Review Letters*, 113:33–39, 1959.

[33] David V Schroeder. *An Introduction to Thermal Physics*. Addison Wesley Longman, 1999.